Elastic Waves at Microwave Frequencies

Mathematical Models using Asymptotic Approximations

John G. Harris
Emeritus, University of Illinois at Urbana-Champaign
Adjunct Professor, Northwestern University
Ctr. QEFP, 2137 N. Sheridan Rd., Evanston, IL 60208-3020
847-491-6236 (voice), j-harris8@northwestern.edu

Preface

This monograph is based on four lectures that were given at the Department of Mathematics and Mechanics, within IIMAS, at the National Autonomous University of Mexico, in Mexico City, during the week beginning 25 January 2004. Lectures two and three have been combined into a single chapter, Chapter 2. Chapter 3 is somewhat different from the lecture given: it is a description of a simpler problem, one that allows the reader to understand some of the details of the calculations. Chapter 1 serves as an introduction to Chapter 2. An Appendix has been added to provide a summary of the equations and other results used in the monograph. References are given that reflect the writer's reading; the list is not comprehensive so that important work has undoubtedly been over-looked.

The purpose in giving these lectures, and in subsequently preparing them for publication, is to make the reader aware of the applied mathematical problems (and opportunities) resulting from the development of transducers that can transmit and receive elastodynamic tone-bursts, whose center frequencies lie in the microwave band. The wavelengths of the elastic waves in this band are tens of micrometers, making the dimensions of most sources, scatterers or waveguides large (with respect to the wavelength). Provided the frequencies do not approach the upper limits of this band, the elastic material can often be approximated as isotropic. The small wavelengths and the assumption of isotropy enable asymptotic methods to be applied to many technically important elastodynamic problems.

One of the more interesting of these problems is constructing a mathematical description of the acoustic imaging of a solid surface. Chapters 1 and 2 describe the writer's asymptotic model of such imaging. It will be shown that an acoustic image of surface features is formed from information carried not only by a specularly reflected wave, but also by one guided by the surface. Therefore, understanding the interaction of these latter waves with surface structures becomes important to modeling mathematically image formation. Chapter 3 describes surface waves propagating in a laterally inhomogeneous elastic layer. This is a beginning to calculating asymptotic

expressions that describe the scattering of surface waves.

The writer enjoyed his visit to IIMAS and learned much. He thanks his host Dr. F. Sabina, and the various faculty and students who participated in the lectures, for giving him the opportunity to gather his ideas on these subjects. Lastly, he thanks Douglas Rebinsky for allowing him to use parts of his dissertation, Gareth Block for his helpful comments on a draft of Chapter 1, and his wife Beatriz for help proofreading the manuscript.

John G. Harris.

Notes

1. The word *phase* is used in a very specific way: the term α is called the phase when it can be written as $\alpha = k\beta$ and appears in an exponential term such as $\exp(\mathrm{i}k\beta)$. When a complex variable $z = |z|\exp(\mathrm{i}\gamma)$ is considered, γ is called the argument.

2. Throughout Chapter 2 the scanned, acoustic imaging device is called a reflection acoustic microscope, or, more simply, an acoustic microscope. This is the common name; however, it is not the most descriptive one. The acoustic imaging device described here is used in many settings. When used for nondestructive evaluation, the operating frequency is on the order of 10 to 100 MHz. Useful images are made, but their resolution is not so great as to merit calling the device a microscope. It only really behaves as a microscope at frequencies on the order of 500 MHz or higher.

3. In Chapter 2 the focal length f is defined as the distance from the plane of the aperture, of the acoustic lens, to the focal point. It can also be defined as the distance from the center of the face of the acoustic lens to the focal point.

Contents

1 The scattering of a spherical wave from a fluid-solid interface **1**

1.1 Description of the problem 1
1.2 Representations for the spherical wave 3
1.3 Scattered wavefields 4
1.4 Wavefield in the fluid 6
1.5 Summary 11

2 Scanned acoustic imaging **13**

2.1 Scanned, reflection acoustic microscope 13
2.2 Fresnel and F-number 15
2.3 Converging spherical wave 16
2.4 Focused acoustic beam 18
2.5 Scattered focused beam 20
2.5.1 Representations 20
2.5.2 Diverging scattered beam, $x_3 < 2z_s$ 22
2.5.3 Converging reflected beam, $2z_s < x_3 < z_s$ 25
2.6 Measurement model 26
2.7 Acoustic material signature 29
2.8 Summary 32

3 Coupled, local elastodynamic modes **33**

3.1 Introduction 33
3.1.1 Description of the problem 34
3.1.2 Background 36
3.1.3 Notation 37
3.2 Rayleigh-Lamb modes 38
3.3 Coupled, local mode approximation 40
3.3.1 A framework for elastic waveguide problems 40
3.3.2 The sloping boundary 42

3.3.3 Coupled, local modes 43
3.4 Coupling of the two lowest Rayleigh-Lamb modes 46
3.4.1 A matrix WKBJ approximation 46
3.4.2 Discussion of the WKBJ approximation 49
3.5 Summary 49

A A miscellany **51**
A.1 Linear elasticity 51
A.2 Linear acoustics 52
A.3 Continuity and boundary conditions 53
A.4 Piezoelectric coupling and an electromechanical reciprocity relation 54
A.5 Notes on Hankel functions 55

Chapter 1

The scattering of a spherical wave from a fluid-solid interface

Abstract

The mathematical description of the waves scattered at a fluid-solid interface, when a spherical acoustic wave strikes it, forms the basis for understanding much about elastic waves in general, and scanned acoustic imaging in particular. By examining this interaction, not only are a number of useful mathematical techniques introduced, but also the underlying physical structure of the scattering phenomena is made manifest. The principal features described in this chapter are: (1) the integral representations of the incident and scattered wavefields, (2) the inter-relation between the analytic structure of the reflection coefficient and the scattered waves, particularly the leaky Rayleigh wave, and (3) the importance of the method of steepest descents in the interpretation of the form of the scattered waves. An angular-spectrum representation of the various wavefields is used.

1.1 Description of the problem

The plane $x_3 = 0$ separates an ideal fluid, in $x_3 < 0$, from a homogenous, isotropic, elastic solid, in $x_3 > 0$, as indicated in Figure 1.1. A unit normal vector $\hat{n} = -\hat{e}_3$ points from the solid into the fluid. A spherical acoustic wave is emitted from a very localized source at $(0, 0, -b)$. When it strikes the fluid-solid interface, part of the spherical wave is reflected, part is transmitted as compressional and shear waves, and part becomes a wave propagating along the interface. The problem, then, is to calculate these scattered waves; the solution is described in this chapter. This solution is

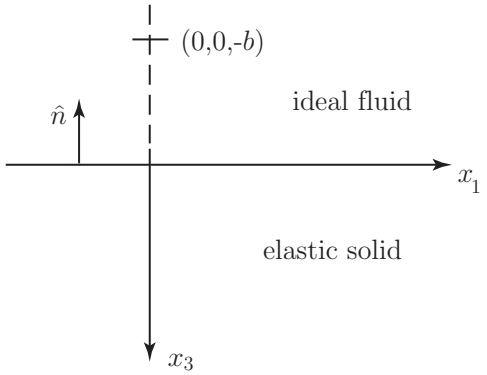

Figure 1.1: The arrangement of the coordinate system. $x_3 > 0$ is occupied by an elastic solid; $x_3 < 0$ is occupied by an ideal fluid. The source is placed at $(0, 0, -b)$, where $b > 0$.

most certainly not new. A detailed one is given in Brekhovskikh and Godin (1999, pp. 1–40), and a more recent reworking of it is given by Pott and Harris (1984). Nevertheless, after examining this problem in this chapter, it will be shown in Chapter 2 that its solution can be progressively reworked so as to describe the imaging mechanism of a scanned acoustic microscope. Here and elsewhere, the wavefields are assumed to be time-harmonic, with an implicit time-dependence $\exp(-\mathrm{i}\omega t)$.

The equation of motion describing small amplitude disturbances in the ideal fluid is given as

$$\nabla^2\varphi + k^2\varphi = -C\,\frac{\delta(r)}{4\pi r^2}, \tag{1.1}$$

where $r = |\mathbf{x} + b\,\hat{e}_3|$ and the wavenumber $k = \omega/c$, with ω being the angular frequency and c the fluid's wavespeed. The particle displacement in the fluid is $\mathbf{u} = \nabla\varphi$, and the acoustic pressure $p = \rho_f\omega^2\varphi$, where ρ_f is the density of the fluid. C is a constant parameter giving the strength of the source at $(0, 0, -b)$. Equation (1.1) is identical to (A.6), when the wave is time-harmonic and the source is a center of dilatation.

The equation of motion describing similar, small amplitude disturbances in the solid is given as

$$\kappa^2\partial_i(\partial_k u_k) - e_{ijk}\partial_j(e_{klm}\partial_l u_m) + k_T^2 u_i = 0. \tag{1.2}$$

The compressional and shear wavenumbers are $k_L = \omega/c_L$ and $k_T = \omega/c_T$, where c_L and c_T are the respective wavespeeds. The parameter $\kappa = c_L/c_T$. Equation (1.2) is an alternative way of writing (A.3); it exhibits the fact

that two wave types, compressional and shear, propagate in an elastic solid (e_{ijk} is the permutation symbol).

The continuity conditions to be satisfied at the interface are, restating (A.7),

$$\mathbf{t}_s \cdot \hat{n} = -p_f, \quad \hat{n} \wedge \mathbf{t}_s = 0, \quad \mathbf{u}_s \cdot \hat{n} = \mathbf{u}_f \cdot \hat{n}, \tag{1.3}$$

where the traction $\mathbf{t}_s = \hat{n} \cdot \boldsymbol{\tau}$. The stress tensor $\boldsymbol{\tau}$ is related to the particle displacement by (A.2). The subscripts s and f indicate properties of the solid and fluid, respectively. Equations (1.1)–(1.3), in combination with the requirement that the scattered waves propagate outward from the interface, constitute the mathematical statement of the problem to be addressed.

1.2 Representations for the spherical wave

Ignoring for the moment the presence of the elastic solid, the solution to (1.1) is

$$\varphi = A\,\frac{e^{\mathrm{i}kr}}{kr}, \quad A = \frac{k\,C}{4\pi}.$$

The constant A has the dimensions of length squared and can be made dimensionless by setting it equal to B/k^2, where B is yet another constant. Following Harris (2001, pp. 24–28), the spherical wave can be written first as

$$\varphi = \frac{\mathrm{i}\,A}{2\pi k} \int_{-\infty}^{\infty} \int_{-\infty}^{\infty} e^{\mathrm{i}(k_1 x_1 + k_2 x_2 + k_3 |x_3 + b|)}\, \frac{dk_1 dk_2}{k_3}, \tag{1.4}$$

where

$$k_3 = (k^2 - k_1^2 - k_2^2)^{1/2}, \quad \Re(k_3) \geq 0,\ \Im(k_3) \geq 0. \tag{1.5}$$

This choice of the branch of k_3 is made so that the spherical wave is outgoing or decays as $|x_3 + b| \to \infty$. And secondly, it can be written as

$$\varphi^i = \frac{\mathrm{i}\,A}{2\pi} \int_0^{2\pi} \int_0^{\pi/2 - \mathrm{i}\infty} e^{\mathrm{i}k\,\hat{p}^{\,i} \cdot \mathbf{x}}\, e^{\mathrm{i}kb\cos\xi}\, \sin\xi\, d\nu\, d\xi, \tag{1.6}$$

where

$$\hat{p}^{\,i} = \sin\xi\,(\cos\nu\,\hat{e}_1 + \sin\nu\,\hat{e}_2) + \cos\xi\,\hat{e}_3\,. \tag{1.7}$$

The superscript i has been added in (1.6), to indicate that this will be the incident spherical wave. Equation (1.6) assumes that $(x_3 + b) > 0$. It was derived using the transformation

$$k_1 = k\sin\xi\cos\nu, \quad k_2 = k\sin\xi\sin\nu, \quad k_3 = k\cos\xi,$$

where the accessible parts of the ξ-plane are determined by the requirement that the spherical wave be outgoing or decay as $|x_3 + b| \to \infty$; that is, the accessible parts of the ξ-plane are taken to agree with (1.5).

Equation (1.6) is referred to as an angular spectrum of plane waves (Clemmow 1966). It is an integration of the plane waves

$$\exp(\mathrm{i}k\,\hat{p}^{\,i}\cdot\mathbf{x})$$

over not only all real directions of propagation, but also over a range of complex directions. If the contour for ξ is taken to be from 0 to $\pi/2$, and then to $(\pi/2 - \mathrm{i}\infty)$, for $\xi \in (\pi/2, \pi/2 - \mathrm{i}\infty)$, $\xi = \pi/2 + \mathrm{i}\xi_2$, with $\xi_2 \leq 0$. In this case the direction given by (1.7) becomes complex:

$$\hat{p}^{\,i} = \cosh\xi_2\,(\cos\nu\,\hat{e}_1 + \sin\nu\,\hat{e}_2) - \mathrm{i}\sinh\xi_2\,\hat{e}_3\,.$$

The imaginary part of $\hat{p}^{\,i}$ produces a decay in the $\hat{e}_3$ direction. The integration over complex angles is essential if the complete curvature of the spherical wave is to be captured by (1.6).

It will be useful to have two additional representations for the spherical wave. Using cylindrical coordinates (ρ, θ, x_3), where $x_1 = \rho\cos\theta$ and $x_2 = \rho\sin\theta$, φ^i can be written as

$$\varphi^i = \frac{\mathrm{i}\,A}{2\pi}\int_0^{\pi/2-\mathrm{i}\infty} e^{\mathrm{i}k\cos\xi\,(x_3+b)}\,\sin\xi\,\left(\int_0^{2\pi} e^{\mathrm{i}k\rho\sin\xi\cos(\nu-\theta)}\,d\nu\right)d\xi.$$

Using the results from Appendix A, §A.5, this integral can be written first as

$$\varphi^i = \mathrm{i}A\int_0^{\pi/2-\mathrm{i}\infty} e^{\mathrm{i}k\cos\xi\,(x_3+b)}\,J_0(k\rho\sin\xi)\sin\xi\,d\xi, \tag{1.8}$$

and secondly as

$$\varphi^i = \frac{\mathrm{i}\,A}{2}\int_{-\pi/2+\mathrm{i}\infty}^{\pi/2-\mathrm{i}\infty} e^{\mathrm{i}k\cos\xi\,(x_3+b)}\,H_0^{(1)}(k\rho\sin\xi)\sin\xi\,d\xi. \tag{1.9}$$

The contour for (1.9) passes above the branch cut for the $H_0^{(1)}$; that cut proceeds from 0 to $(-\pi/2 - \mathrm{i}\infty)$. Both representations are integrals over cylindrical waves. Equation (1.9) is very useful when calculating an asymptotic expansion to φ^i.

1.3 Scattered wavefields

Consider briefly the expressions for the plane waves reflected and transmitted at a fluid-solid interface when a plane wave, incident from the fluid,

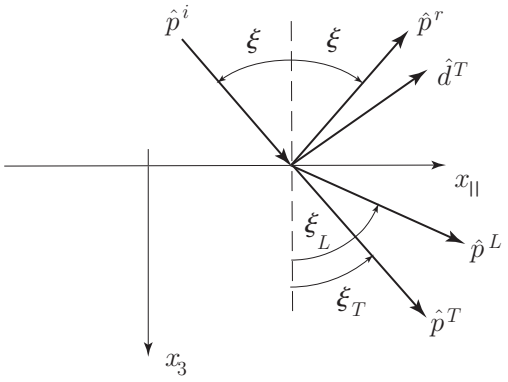

Figure 1.2: The geometry of the incident and scattered rays. The incident and scattered propagation vectors are shown, as is the polarization vector $\hat{d}^T$. Moreover, the angles ξ, ξ_L, and ξ_T are indicated.

strikes it. Harris (2001, pp. 37-55) indicates one way to calculate these waves. Reflection and transmission, and their respective coefficients are calculated using the particle displacement $\mathbf{u}$, rather than the potential φ; this makes the wave phenomena in the solid somewhat easier to understand. Each plane wave is characterized by a unit propagation vector $\hat{p}$ and a unit polarization vector $\hat{d}$, so that the incident plane wave is written as

$$\mathbf{u}^i = \hat{d}^i \, e^{\mathrm{i}k\,\hat{p}^i\cdot\mathbf{x}}, \quad \hat{d}^i = \hat{p}^i,$$

where $\hat{p}^i$ is given by (1.7). The reflected and transmitted waves must all phase-match to the incident wave; thus,

$$k \sin\xi = k_L \sin\xi_L = k_T \sin\xi_T,$$

where the angles ξ_L and ξ_T are indicated in Figure 1.2. These waves are given by

$$\begin{aligned}
\mathbf{u}^r &= R(\xi)\,\hat{d}^r \, e^{\mathrm{i}k\,\hat{p}^r\cdot\mathbf{x}}, \quad \hat{d}^r = \hat{p}^r, \quad \hat{p}^r = \sin\xi\,\hat{e}_{||} - \cos\xi\,\hat{e}_3, \\
\mathbf{u}^L &= T_L(\xi)\,\hat{d}^L \, e^{\mathrm{i}k\,\hat{p}^L\cdot\mathbf{x}}, \quad \hat{d}^L = \hat{p}^L, \quad \hat{p}^L = \sin\xi_L\,\hat{e}_{||} + \cos\xi_L\,\hat{e}_3, \\
\mathbf{u}^T &= T_T(\xi)\,\hat{d}^T \, e^{\mathrm{i}k\,\hat{p}^T\cdot\mathbf{x}}, \quad \hat{p}^T \wedge \hat{d}^T = \hat{e}_T, \quad \hat{p}^T = \sin\xi_T\,\hat{e}_{||} + \cos\xi_T\,\hat{e}_3.
\end{aligned} \tag{1.10}$$

Two new unit vectors

$$\hat{e}_{||} = \cos\nu\,\hat{e}_1 + \sin\nu\,\hat{e}_2, \quad \hat{e}_T = \hat{e}_3 \wedge \hat{e}_{||}.$$

have been introduced. The superscripts r, L, and T indicate the reflected, transmitted longitudinal, and transmitted transverse waves, respectively. The reflection and transmission coefficients, $R(\xi)$ and $T_{L,T}(\xi)$, respectively, are given as

$$R(\xi) = \frac{A_-(\xi)}{A_+(\xi)}, \quad T_L(\xi) = \frac{2\kappa\,\kappa_f\,(\rho_f/\rho_s)\cos\xi\cos(2\xi_T)}{A_+(\xi)},$$

$$T_T(\xi) = -\,\frac{2\kappa_f\,(\rho_f/\rho_s)\cos\xi\sin(2\xi_L)}{A_+(\xi)}, \tag{1.11}$$

where

$$A_\pm = \cos\xi[\sin(2\xi_L)\sin(2\xi_T) + \kappa^2\cos(2\xi_T)] \pm \kappa\,\kappa_f\,(\rho_f/\rho_s)\cos\xi_L. \tag{1.12}$$

The parameter $\kappa_f = c/c_T$. Recall that $\kappa = c_L/c_T$.

Returning to the problem under discussion and using (1.6), the incident wave becomes

$$\mathbf{u}^i = -\frac{k\,A}{2\pi}\int_0^{2\pi}\int_0^{\pi/2-\mathrm{i}\infty} \hat{d}^{\,i}(\xi,\nu)\,e^{\mathrm{i}k\,\hat{p}^{\,i}\cdot\mathbf{x}}\,e^{\mathrm{i}kb\cos\xi}\,\sin\xi\,d\nu\,d\xi.$$

Noting that the problem is linear and that the scattered plane waves are given by (1.10), the waves scattered from the interface are directly calculated to give the equations

$$\mathbf{u}^r = -\frac{k\,A}{2\pi}\int_0^{2\pi}\int_0^{\pi/2-\mathrm{i}\infty} \hat{d}^{\,r}(\xi,\nu)R(\xi)\,e^{\mathrm{i}k\,\hat{p}^{\,r}\cdot\mathbf{x}}\,e^{\mathrm{i}kb\cos\xi}\,\sin\xi\,d\nu\,d\xi, \tag{1.13}$$

and

$$\mathbf{u}^{L,T} = -\frac{k\,A}{2\pi}\int_0^{2\pi}\int_0^{\pi/2-\mathrm{i}\infty} \hat{d}^{\,L,T}(\xi,\nu)T_{L,T}(\xi)\,e^{\mathrm{i}k_{L,T}\,\hat{p}^{\,L,T}\cdot\mathbf{x}}\,e^{\mathrm{i}kb\cos\xi}\,\sin\xi\,d\nu\,d\xi.$$

Equation (1.10) lists the propagation and polarization vectors. It should be clear to the reader that all further outcomes depend on the analytic structure of the phases in the integrands and of $A_\pm(\xi)$.

1.4 Wavefield in the fluid

For the remainder of this chapter only the wavefield in the fluid, (1.13), will be considered, because it is the wavefield used to form an image by a

scanning acoustic microscope. Using the transformation that yielded the representation (1.9), $\mathbf{u}^r$ is written as

$$\mathbf{u}^r = \frac{\mathrm{i}\,A}{2}\,\nabla \int_{-\pi/2+\mathrm{i}\infty}^{\pi/2-\mathrm{i}\infty} R(\xi)\, e^{\mathrm{i}k(b-x_3)\cos\xi}\, H_0^{(1)}(k\rho\sin\xi)\sin\xi\, d\xi. \qquad (1.14)$$

Recall that cylindrical coordinates (ρ, θ, x_3), where $x_1 = \rho\cos\theta$ and $x_2 = \rho\sin\theta$, are introduced to arrive at this representation. Noting the Sommerfeld representation of $H_0^{(1)}$, given in §A.5, it is seen that (1.14) is a double integral whose phase is

$$\Phi(\xi, \mu) = (b - x_3)\cos\xi + \rho\sin\xi\cos\mu.$$

Note: The second, mixed derivative $\partial_\xi\partial_\mu\Phi = 0$ when evaluated at the stationary point (ξ^*, μ^*), where $(b - x_3)\sin\xi^* = \rho\cos\xi^*$ and $\mu^* = 0$. As a consequence, (1.14) can be treated as an iterated integral, to leading order, when asymptotically approximating it.

Using the asymptotic approximation for $H_0^{(1)}$ given in §A.5, and introducing the spherical coordinates (r, ϕ, θ), where $(b - x_3) = r\cos\phi$ and $\rho = r\sin\phi$, (1.14) can be approximated as

$$\mathbf{u}^r \sim -\frac{kA}{2}\left(\frac{2}{\pi k\rho}\right)^{1/2} e^{-\mathrm{i}\pi/4} \int_{\mathcal{C}(\phi)} \hat{d}^r(\xi) R(\xi)\, e^{\mathrm{i}kr\cos(\xi-\phi)}\,(\sin\xi)^{1/2}\, d\xi, \qquad k\rho \to \infty. \quad (1.15)$$

The phase of the integrand of (1.15) has a stationary point at $\xi = \phi$. The contour $\mathcal{C}(\phi)$ is the steepest descents contour; Figure 1.3 (b) is a sketch of a part of this contour as it passes through ϕ. The method of steepest descents is described in Felsen and Marcuvitz (1994, pp. 370–391) and Harris (2001, pp. 91–94). Lastly, note that the dependence on ν in $\hat{d}^r$ has been dropped because it is clear, at this point, that the wavefield is axisymmetric.

The subsequent asymptotic approximation of this integral depends on the proximity of ϕ to the poles and branch points of $R(\xi)$. $A_+(\xi)$, which is given by (1.12), has four zeros, $\pm\xi_R$ and $\pm\xi_S$, and four branch points, $\pm\xi_{bL}$ and $\pm\xi_{bT}$. The branch points are defined by the equations

$$\sin\xi_{bL} = c/c_L, \quad \sin\xi_{bT} = c/c_T.$$

Figure 1.3 (a) shows the right-half of the complex ξ-plane with these poles and branch points indicated. The poles of $R(\xi)$ correspond to leaky Rayleigh waves ($\pm\xi_R$), and Stoneley waves ($\pm\xi_S$); and the branch points to various

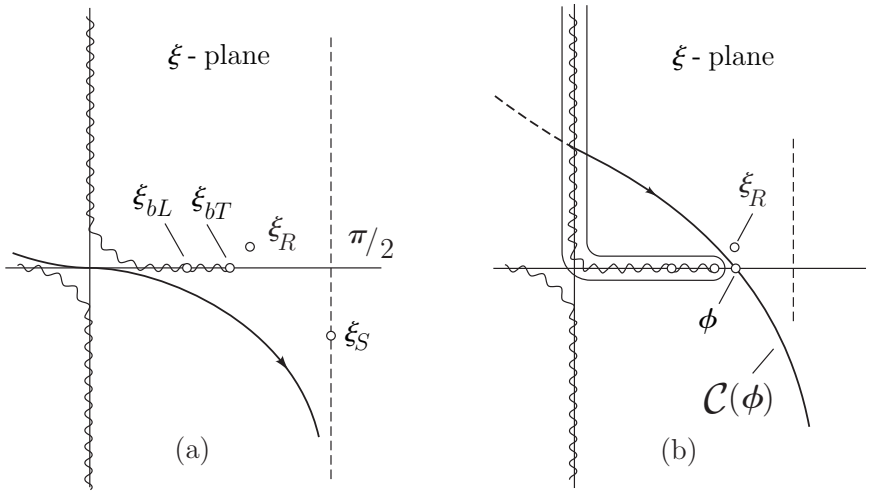

Figure 1.3: The structure of the complex ξ-plane for $\Re(\xi) \geq 0$. (a) The contour for (1.14), the branch cuts beginning at the branch points ξ_{bL} and ξ_{bT}, the leaky Rayleigh pole ξ_R, and the Stoneley pole ξ_S are indicated. (b) The steepest descents contour $\mathcal{C}(\phi)$ of (1.15) is sketched. The spatial relation between the steepest descents contour and the leaky Rayleigh pole ξ_R is shown.

lateral waves. The wiggly lines in Figure 1.3 indicate the branch cuts corresponding to these branch points. These cuts, which define the Riemann sheet on which the problem is solved, are determined by demanding that $\Im(\cos\xi_I) \geq 0,\ \ I = L, T$, everywhere on the Riemann sheet of interest. Because $R(\xi)$ is a reflection coefficient for an incident plane wave, the branch cuts are chosen to ensure that when critical refraction takes place in the solid, the refracted waves decay with depth.

In this chapter only the effect of the leaky Rayleigh-wave pole is considered, and only a *nonuniform asymptotic expansion* is given. A nonuniform expansion, in the present context, is one that does not accurately account for what happens when the stationary point lies in the neighborhood of a pole, a branch point, or both a pole and a branch point. In these cases $R(\xi)$ varies rapidly making the usual steepest descents approximation inaccurate.

Some of the consequences of seeking a uniform expansion, as ϕ coalesces with each of these critical points separately, are explored in Pott and Harris (1984), and Harris and Pott (1985). A case not explored in these papers is that in which the stationary point ϕ, the pole ξ_R, and branch pointξ_{bT} coalesce. A method to do so is described in Ciarkowski (1989).

A nonuniform asymptotic approximation to (1.15) is given as

$$\mathbf{u}^r \sim u^g\, \hat{d}^r(\phi) + \chi(\xi_R, \phi)\, u^R\, \hat{d}^r(\xi_R), \quad kr \to \infty, \tag{1.16}$$

where

$$\chi(\xi_R, \phi) = \begin{cases} 1 & \text{if } \mathcal{C}(\phi) \text{ encloses } \xi_R, \\ 0 & \text{otherwise.} \end{cases}$$

The polarization vector $\hat{d}^r(\phi)$ is given by (1.10) with ξ replaced by ϕ; similarly, the polarization vector $\hat{d}^r(\xi_R)$ is given by (1.10) with ξ replaced by ξ_R. The specularly reflected spherical wave u^g is given as

$$u^g = \mathrm{i}kA\, R(\phi)\, \frac{e^{\mathrm{i}kr}}{kr}. \tag{1.17}$$

Note that the condition that $k\rho \to \infty$, used in (1.15), does not influence the final outcome describing u^g; that is, (1.17) remains accurate even as $\rho \to 0$.

Describing u^R requires somewhat more detail. The leaky Rayleigh pole is

$$\xi_R = \beta_R + \mathrm{i}\alpha_R, \quad \beta_R, \alpha_R > 0. \tag{1.18}$$

In all cases of interest here $\alpha_R/\beta_R \ll 1$. Somekh et al. (1985) show that

$$\frac{A_-(\xi_R)}{dA_+/d\xi(\xi_R)} \approx 2\mathrm{i}\alpha_R. \tag{1.19}$$

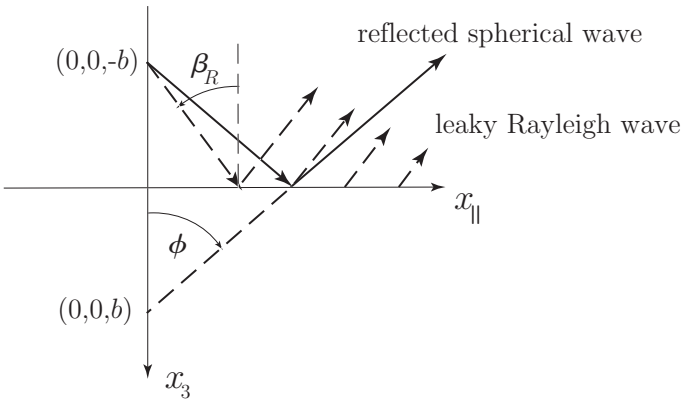

Figure 1.4: A drawing indicating the nature of the leaky Rayleigh wave excited by a ray incident at the angle β_R. Also shown is the ray describing the reflected wave being emitted from the image point $(0, 0, b)$

This approximation will be used very frequently. Moreover, except in the phase terms, the approximation $\xi_R \approx \beta_R$ is used. Again noting the various unit vectors introduced in (1.10), the unit vectors $\hat{p}^R$ and $\hat{d}^R$, given by the expressions

$$\hat{p}^R = \sin\beta_R\,\hat{e}_\parallel - \cos\beta_R\,\hat{e}_3, \quad \hat{p}^R \wedge \hat{d}^R = \hat{e}_T,$$

are introduced. Note that $\hat{d}^r(\xi_R) \approx \hat{p}^R$. Incorporating these approximations and the newly defined unit vectors, u^R can be expressed as

$$u^R = kA\left(\frac{2\pi}{kr_R}\right)^{1/2} 2\alpha_R\, e^{-\mathrm{i}\pi/4}\, e^{\mathrm{i}k\hat{p}^R\cdot\mathbf{x}\,\cosh\alpha_R} \times e^{\mathrm{i}kb\cos\beta_R\,\cosh\alpha_R}\, e^{k\hat{d}^R\cdot\mathbf{x}\,\sinh\alpha_R}\, e^{kb\sin\beta_R\,\sinh\alpha_R}, \tag{1.20}$$

where $r_R = \rho/\sin\beta_R$.

Equation (1.20) describes an inhomogeneous wave propagating away from the interface in the direction $\hat{p}^R$, and decaying in the direction $-\hat{d}^R$. The possibility of unlimited growth in the direction $\hat{d}^R$ is removed from $\mathbf{u}^r$, (1.16), by the indicator function $\chi(\xi_R, \phi)$. Viewing it in the coordinates indicated in Figure 1.1, (1.20) describes a Rayleigh surface wave that steadily radiates, or leaks, into the fluid so that, as it propagates along the interface, it also decays. Further, it only appears outside a right circular cone whose vertex is at $(0, 0, b)$, and which opens upward cutting the surface, at $x_3 = 0$, in a circle of radius $b\cot\beta_R$. Figure 1.4 is a drawing that attempts to indicate these relationships.

1.5 Summary

1. Equations (1.16), (1.17), and (1.20) are the principal results of this chapter. They describe the most important waves scattered from the fluid-solid interface, namely, the specularly reflected spherical wave and the leaky Rayleigh wave.

2. By using the angular spectrum representation of the incident wave, (1.6), representations of the reflected wavefield, (1.13), and the transmitted wavefields were readily calculated; and expressed in a form that indicated the underlying role of the scattering of a plane wave. Moreover, these representations indicated that many of the physical outcomes of the problem could be inferred directly from the analytic behavior of the reflection and transmission coefficients.

3. Representations of the spherical wave as an integral over cylindrical waves, (1.8) and (1.9), were also given. Equation (1.8) exhibits the spherical wave as an inverse Hankel transform; equation (1.9) proved quite useful in calculating the asymptotic approximation begun with (1.14).

Chapter 2

Scanned acoustic imaging

Abstract

An angular spectrum representation of a converging spherical wave is derived, and then combined with a similar representation for a diverging spherical wave to construct a model of a focused acoustic beam. This beam is directed at a fluid-solid interface and the scattered wavefield calculated, much as was done in Chapter 1. Representations of the incident and scattered wavefields are also expressed as Hankel transforms.

A model of the scanned acoustic microscope is next constructed. Using an electromechanical reciprocity relation, the following imaging equation is derived:

$$\delta V(\mathbf{s}, z_s) = 2\mathrm{i}D \int_0^{\beta_a} G^2(\xi)\, R(\xi, \mathbf{s}) e^{\mathrm{i}2kz_s \cos\xi}\, d\xi.$$

This expression maps the mechanical reflection coefficient $R(\xi, \mathbf{s})$ to the measured change in voltage $\delta V(\mathbf{s}, z_s)$. This change depends on the lateral position of the microscope $\mathbf{s}$, and the relative distance z_s between the geometrical focal plane and the interface, that is being imaged. The function $G(\xi)$ and angle β_a describe how the finite aperture of the lens limits the acquisition of information. Varying $\mathbf{s}$ produces an image, while varying z_s allows the device to be used as an interferometer.

2.1 Scanned, reflection acoustic microscope

Figure 2.1 shows the acoustic microscope that will be modeled in this chapter. A piezoelectric transducer is placed at one end of a buffer rod and an acoustic lens is ground into the opposite end, as shown in Figure 2.1(a). The transducer, when excited by a tone-burst converts the incident electromagnetic wave into an elastic compressional wave that propagates down

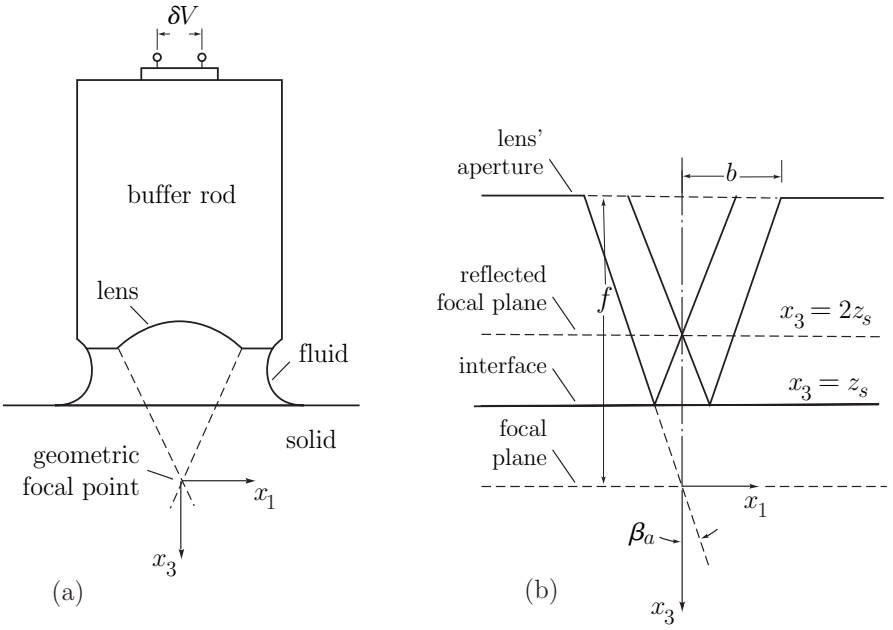

Figure 2.1: (a) A drawing of the transducer, buffer rod and lens of the acoustic microscope. Note that the origin of the coordinate system is placed at the geometrical focal point. (b) A drawing of the principal geometrical features of the region between the plane of the lens' aperture and the geometric focal plane. Note that in this arrangement $z_s < 0$.

the buffer rod to the lens. It is transmitted through a lens into a coupling fluid. If the overall region being scanned is small the fluid is little more than a drop at the end of the buffer rod, as suggested in the figure, while, if the region being scanned is large, then the whole device is immersed in the fluid. The lens focuses the sound at or near the fluid-solid interface. An echo is excited and subsequently collected by the lens. It propagates back through the buffer rod to the transducer where it is converted into an electromagnetic wave. The buffer rod introduces a time delay between the initial excitation and the echo, allowing the two to be separated. The buffer rod, with its transducer and lens, is mechanically scanned, in a raster pattern, across the interface. The echo at each point, after being converted to an electrical signal, is displayed as a dot on a screen, having a color or level of grey determined by its strength. The total of all the dots acquired during the scan is the image.

As will become apparent, the microscope can also be used as an interferometer. As was shown in Chapter 1, a leaky Rayleigh surface wave is also excited at the interface. It is collected along with the reflected wave and both waves are added together by the transducer. If the geometrical focal point is placed below the interface, in the solid, at a distance z_s, as shown in Figure 2.1(b), then the signal received from the transducer exhibits interference, between the reflected wave and the leaky Rayleigh wave, as z_s is varied.

The work of this chapter is based on two papers by Rebinsky and Harris (1992b, Rebinsky and Harris (1992a), and a Ph. D. dissertation by Rebinsky (1991). Many of the figures shown in this chapter are taken from this dissertation. These references also discuss the role of the leaky Rayleigh wave in enhancing images of surface-breaking cracks, something not written about here. A somewhat broader overview of mathematically modelling acoustic imaging in solids is provided by the review article Harris (1997). The monograph by Briggs (1992) gives a comprehensive overview of acoustic microscopy, at higher frequencies, along with many interesting photographs. Note that the derivation given in Briggs (1992, pp. 109–123) of the imaging equation differs from that described here. The approach of Rebinsky and the writer was initially motivated by Liang, Kino, and Khuri-Yakub (1985).

2.2 Fresnel and F-number

If one examines how an optical plane wave diffracts at a circular aperture and then how it is made to focus by a lens embedded in that same aperture — a particularly good reference describing this is Born and Wolf (1999, pp. 484–

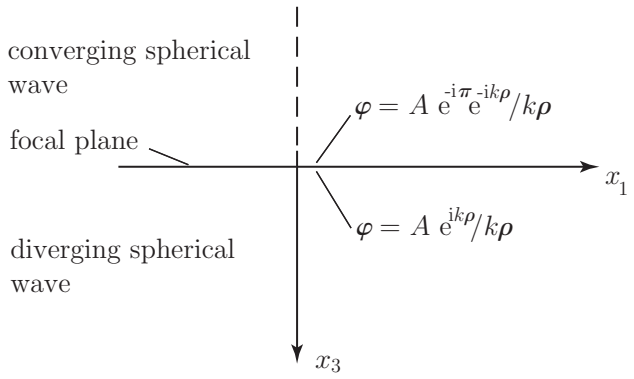

Figure 2.2: The arrangement of the coordinate system. The form taken by the converging and diverging spherical wave on each side of the focal plane at $x_3 = 0$ is indicated. Note that there is a phase jump of π across this plane.

503) — one will discover the following facts: At the Fresnel distance, a plane wave transmitted through an aperture and the waves diffracted by its edges begin to merge; it is here that a beam is formed (Harris 1989). If b is the aperture radius, and k the wavenumber, the Fresnel distance is $kb^2/(2\pi)$. Placing a lens in the aperture converts the transmitted plane wave into a spherical wave converging to a point, a distance f away; f is the focal length. The waves diffracted by the edges continue to be present. The resulting wavefield depends critically on whether or not focusing is made to occur before or after the edge-diffracted waves merge with the converging spherical one. The Fresnel number $N = kb^2/(2\pi f)$ is a measure of this, and is an important number characterizing an imaging system. A second one is the F-number, where $F = f/b$. Note that $kb/(2\pi) = N\,F$. The scanned acoustic microscope considered in this chapter is such that $N \gg 1$ and $F \approx 1$. This makes the scaled radius of the aperture, kb, large.

2.3 Converging spherical wave

A mathematical description of a focused acoustic beam is constructed in this and the next section. To begin, the idealized case of a spherical wave converging to a point and then diverging to infinity is first described. Figure 2.2 indicates the geometry: The x_3-axis is the centerline. A spherical wave in $x_3 < 0$ converges to the origin and then, in $x_3 > 0$, diverges to infinity. In crossing the plane $x_3 = 0$ it is made to undergo a phase jump of π. It is

known that focused beams experience such a phase jump, though, the phase variation occurs more gradually within a finite focal region (Born and Wolf 1999, pp. 494–499).

Equations (1.6) and (1.7), with $b = 0$, describe an outgoing or diverging spherical wave in $x_3 > 0$. Equation (1.6) is repeated here:

$$\varphi = \frac{\mathrm{i}\,A}{2\pi} \int_0^{2\pi} \int_0^{\pi/2-\mathrm{i}\infty} e^{\mathrm{i}k\,\hat{p}^{\,i}\cdot\mathbf{x}} \sin\xi \, d\nu \, d\xi. \tag{2.1}$$

At $x_3 = 0^+$, φ reduces to

$$\varphi = A\frac{e^{\mathrm{i}k\rho}}{k\rho},$$

where $x_1 = \rho\cos\theta$ and $x_2 = \rho\sin\theta$. Equation (2.1) describes a diverging spherical wave in $x_3 > 0$; the accessible regions of the ξ-plane, as $x_3 \to \infty$ are those for which $\Re(\cos\xi) \geq 0$ and $\Im(\cos\xi) \geq 0$. Recall that $k_3 = k\cos\xi$, so that these conditions are equivalent to those in (1.5).

To construct the incoming or converging spherical wave, in $x_3 < 0$, φ is written as

$$\varphi = \frac{1}{(2\pi)^3} \int_{-\infty}^{\infty} \int_{-\infty}^{\infty} {}^*\varphi(k_1, k_2) e^{\mathrm{i}(k_1x_1+k_2x_2+k_3x_3)} \, \frac{dk_1 dk_2}{k_3}, \tag{2.2}$$

where

$$k_3 = (k^2 - k_1^2 - k_2^2)^{1/2}, \quad \Re(k_3) \geq 0, \ \Im(k_3) \leq 0; \tag{2.3}$$

Note that the definition of k_3 has changed from that given by (1.5). The changed definition ensures that, as $x_3 \to -\infty$, the exponential term decays or acts as an incoming plane wave. The transform ${}^*\varphi$ is determined by asking that at $x_3 = 0^-$, φ be given by the expression (see Figure 2.2)

$$\varphi = Ae^{-\mathrm{i}\pi}\frac{e^{-\mathrm{i}k\rho}}{k\rho}.$$

It is found that

$${}^*\varphi = \frac{\mathrm{i}2\pi A}{kk_3}.$$

Again introducing the transformation

$$k_1 = k\sin\xi\cos\nu, \quad k_2 = k\sin\xi\sin\nu, \quad k_3 = k\cos\xi,$$

the angular spectrum representation of the converging spherical wave is given as

$$\varphi = \frac{\mathrm{i}\,A}{2\pi} \int_0^{2\pi} \int_0^{\pi/2+\mathrm{i}\infty} e^{\mathrm{i}k\,\hat{p}^{\,i}\cdot\mathbf{x}} \sin\xi \, d\nu \, d\xi, \tag{2.4}$$

where $\hat{p}^{\,i}$ is given by (1.7), but is repeated here:

$$\hat{p}^{\,i} = \sin\xi\,(\cos\nu\,\hat{e}_1 + \sin\nu\,\hat{e}_2) + \cos\xi\,\hat{e}_3\,.$$

The accessible parts of the ξ-plane, as $x_3 \to -\infty$, are determined by the definition of k_3, given by (2.3), which implies that $\Re(\cos\xi) \geq 0$ and $\Im(\cos\xi) \leq 0$. In fact the only apparent difference between the diverging spherical wave, (2.1), and the converging one, (2.4), arises from the definition of k_3 and the contour of integration for ξ.

2.4 Focused acoustic beam

A focused wave constructed from a converging and diverging spherical wave is not physically realizable. First, a spherically converging wave could not be excited because it would demand that all the plane waves in its spectrum, including those propagating at complex angles, be available at some initial aperture. Secondly, the wavefield in the focal plane should be continuous and not have a jump in phase of π. Such a change is permissible in the sense that between the source of the converging wave and the far-field of the diverging wave a net phase change of π may occur, but the change should not cause a discontinuity at the focal plane. Using intuition, and the knowledge gained from constructing the representations of the converging and diverging spherical waves, the following is proposed as a model of a focused acoustic beam:

$$\varphi^i = \frac{\mathrm{i}\,A}{2\pi}\int_0^{2\pi}\int_0^{\pi/2} G(\xi) e^{\mathrm{i}k\,\hat{p}^{\,i}\cdot\mathbf{x}}\,\sin\xi\,d\nu\,d\xi. \tag{2.5}$$

By eliminating the complex legs of the contours, the sudden jump at $x_3 = 0$ has been eliminated, and by introducing a function $G(\xi)$ the focal region at the origin has been modulated to capture more accurately the fact that radiation cannot be focused to a point. The function $G(\xi)$ is defined so that it is symmetric in its argument ξ and is nonzero for $\xi \in (-\pi/2, \pi/2)$. Lastly, a superscript i has been added because, in subsequent sections, (2.5) will become the incident focused beam emitted from the lens' aperture.

Two additional representations of (2.5) are useful. Using the results from Appendix A §A.5, the first is

$$\varphi^i = \mathrm{i}A\int_0^{\pi/2} G(\xi)\,e^{\mathrm{i}kx_3\cos\xi}\,J_0(k\rho\sin\xi)\sin\xi\,d\xi, \tag{2.6}$$

and the second is

$$\varphi^i = \frac{\mathrm{i}A}{2}\int_{-\pi/2}^{\pi/2} G(\xi)\,e^{\mathrm{i}kx_3\cos\xi}\,H_0^{(1),(2)}(k\rho\sin\xi)\sin\xi\,d\xi. \tag{2.7}$$

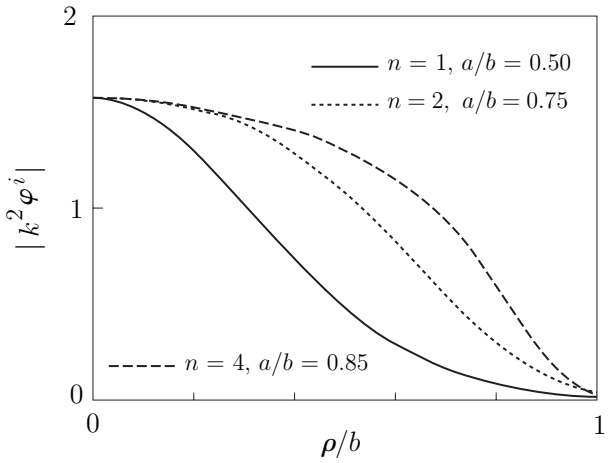

Figure 2.3: The distribution of the wavefield over an imagined aperture at $|x_3| = f$. A is selected arbitrarily to give the vertical scale shown. The parameters n and a/b measure how fully the converging spherical wave fills the aperture

The Hankel function $H_0^{(1)}$ is selected when $x_3 > 0$. Its branch cut proceeds from 0 to $(-\pi/2 - \mathrm{i}\infty)$; the integration contour passes above it. The Hankel function $H_0^{(2)}$ is selected when $x_3 < 0$. Its branch cut proceeds from 0 to $(-\pi/2 + \mathrm{i}\infty)$; the integration contour passes below it.

The function $G(\xi)$ is specified by asking that, far from the focal plane, in the half-space $x_3 < 0$, φ match a prescribed wavefield. This wavefield is thought of as that which fills an aperture, of radius b, placed at a distance $|x_3| = f$ from the focal plane. It is specified as

$$\varphi^i = -H(b-\rho)\, A\, e^{(\rho/a)^{2n}}\, \frac{e^{-\mathrm{i}kr}}{kr}, \tag{2.8}$$

where $H(x)$ is the Heaviside step function, and $r = (\rho^2 + x_3^2)^{1/2}$. Note that the aperture is filled with a converging spherical wave. Recall that $x_1 = \rho\cos\theta$ and $x_2 = \rho\sin\theta$. The coordinate ϕ has been introduced such that $\phi \in [0, \pi/2)$; and $\rho = r\sin\phi$, and $|x_3| = r\cos\phi$. The parameters a and n, where n is a positive integer, allow one to describe how fully the incident wavefield fills the aperture. Figure 2.3 shows three profiles for various values of a/b and n. The larger a/b the more the wavefield fills the aperture, and the larger n the more the function resembles a top-hat.

Equation (2.7) is asymptotically approximated as $kr \to \infty$ using a pro-

cedure identical to that used in §1.4 to approximate the wavefield scattered into the fluid. This approximation gives

$$\varphi^i \sim \mp A\, G(\phi) \frac{e^{\mp \mathrm{i}kr}}{kr}, \quad kr \to \infty,\ x_3 \lesseqgtr 0. \tag{2.9}$$

Matching (2.9) with (2.8) gives

$$G(\phi) = H(\beta_a - \phi)\, \exp\left[-\left(\frac{f \tan\phi}{a} \right)^{2n} \right], \quad \phi \in [0, \pi/2). \tag{2.10}$$

The angle β_a is defined as $\cot \beta_a = F$. Equations (2.5) and (2.10) together define the model of a focused beam to be used here.

Note that the choice of the wavefield in the aperture is such that edge-diffracted waves are almost eliminated. This choice was based on the observation that the microscope's acoustic lens did not have sharp edges; instead the edges were smoothed out. Accordingly, it was reasoned that only weak edge-diffraction occurred.

2.5 Scattered focused beam

2.5.1 Representations

The reflection of the focused beam is needed next. It is calculated in much the same way as was done in Chapter 1, §1.4 and §1.5. Noting that the incident focused beam (2.5) is an integral over plane waves, an integral representation of the reflected focused beam can be written down as

$$\varphi^r = \frac{\mathrm{i}A}{2\pi} \int_0^{2\pi} \int_0^{\pi/2} G\xi) R(\xi) e^{\mathrm{i}k\,\hat{p}^{\,r}\cdot\mathbf{x}}\, e^{\mathrm{i}2kz_s \cos\xi}\, \sin\xi\, d\nu\, d\xi. \tag{2.11}$$

The propagation vector $\hat{p}^{\,r}$ is given by (1.10), but is repeated here:

$$\hat{p}^{\,r} = \sin\xi(\cos\nu\, \hat{e}_1 + \sin\nu\, \hat{e}_2) - \cos\xi\, \hat{e}_3.$$

The plane-wave reflection coefficient $R(\xi)$ is given by (1.11) and (1.12). It is important to recall the branch cuts for $R(\xi)$ in the ξ-plane; these are discussed in the paragraph following (1.15) and partially indicated by Figure 1.3. These cuts determine the Riemann sheet on which the contour of integration of (2.11) is taken; the integration contour passes below the branch cuts whose branch points are ξ_{bL} and ξ_{bT}.

To interpret (2.11) it is helpful to refer to Figure 2.1(b). First recall that the origin of the coordinate system for the focused beam is the geometrical

focal point, which in Figure 2.1(b) is a distance $|z_s|$ from the interface. If the incident beam strikes the interface before it focuses, then its reflection focuses in a reflected focal plane at $x_3 = 2z_s$, the mirror image of the focal plane. Combining the phase terms, a distance $|x_3 - 2z_s|$ emerges indicating that, for $2z_s < x_3 < z_s$, (2.11) represents a beam converging to $(0, 0, 2z_s)$, while, for $x_3 < 2z_s$, it represents a beam diverging from $(0, 0, 2z_s)$.

Again two additional representations of (2.11) are useful. Using the results from §A.5, the first is

$$\varphi^r = \mathrm{i}A \int_0^{\beta_a} G(\xi)R(\xi)\, e^{-\mathrm{i}k(x_3-2z_s)\cos\xi}\, J_0(k\rho\sin\xi)\sin\xi\, d\xi. \tag{2.12}$$

The second is similar to (2.7). However, this representation will be used to asymptotically approximate the reflected wavefield; thus, it is important to scale the variables to identify what parameter is large. The scaled variables $\bar\rho = \rho/b$, $\bar x_3 = x_3/f$, and $\bar z_s = z_s/f$ are introduced. This gives the second representation as

$$\varphi^r = \frac{\mathrm{i}A}{2} \int_{-\beta_a}^{\beta_a} G(\xi)R(\xi)\, e^{-\mathrm{i}kbF(\bar x_3-2\bar z_s)\cos\xi}\, H_0^{(1),(2)}(kb\bar\rho\sin\xi)\sin\xi\, d\xi. \tag{2.13}$$

The Hankel function $H_0^{(1)}$ is selected when $x_3 < 2z_s$. In this case the contour passes above the branch cut for $H_0^{(1)}$, whose cut proceeds from 0 to $(-\pi/2 - \mathrm{i}\infty)$. It also passes above the branch cuts of $R(\xi)$, whose branch points are $-\xi_{bL}$ and $-\xi_{bT}$, and below those whose branch points are ξ_{bL} and ξ_{bT}. This is a beam diverging from the reflected focal plane. The Hankel function $H_0^{(2)}$ is selected when $2z_s < x_3 < z_s$. The contour passes *below* the branch cut for the Hankel function, which proceeds from 0 to $(-\pi/2 + \mathrm{i}\infty)$. However, it passes *above* the branch cuts of $R(\xi)$, whose branch points are $-\xi_{bL}$ and $-\xi_{bT}$, and below those whose branch points are ξ_{bL} and ξ_{bT}. This is a beam converging toward the reflected focal plane.

Recalling the discussion of §2.2, $F \approx 1$ and $kb \gg 1$. Therefore, the integral (2.13) can be asymptotically approximated in the same way as was $\mathbf{u}_r$ in §1.4, though in this case kb has been explicitly identified as the large parameter. However, proceeding in this way will lead to an unexpected difficulty for the case of the reflected converging beam. It will become apparent that, when the reflected focal plane lies above it, leaky Rayleigh waves are excited at the interface that focus at $\rho = 0$. Therefore, the asymptotic approximation in this latter case must be modified somewhat from that described in §1.4.

2.5.2 Diverging scattered beam, $x_3 < 2z_s$

Where $x_3 < 2z_s$, the asymptotic approximation for $H_0^{(1)}$, taken from §A.5, is introduced into (2.13). As well, the spherical coordinates (r, ϕ, θ) are introduced by setting $\rho = r \sin\phi$ and $|x_3 - 2z_s| = r\cos\phi$ (θ never appears because the wavefields are axisymmetric about the x_3-axis). Note that $\phi \in [0, \pi/2)$. Equation (2.13) is thus approximated as

$$\varphi^r \sim \frac{\mathrm{i}A}{2}\left(\frac{2}{\pi kb\bar{\rho}}\right)^{1/2} e^{\mathrm{i}\pi/4} \int_{-\beta_a}^{\beta_a} G(\xi)R(\xi)\, e^{\pm \mathrm{i}kbF\bar{r}\cos(\xi-\phi)} \sin^{1/2}\xi \, d\xi, \qquad kb \to \infty, \quad (2.14)$$

where $\bar{r} = r/f$.

Equation (2.14) is very similar to (1.15). The steepest descents contour for this case is identical to that shown in Figure 1.3(b). The contributions from the end points at $\pm\beta_a$ are not significant, primarily because $G(\beta_a)$ is small. Carrying out the approximation gives

$$\varphi^r \sim \varphi^g + \chi_d(\xi_R, \phi)\, \varphi^R, \quad kb \to \infty, \qquad (2.15)$$

where

$$\chi_d(\xi_R, \phi) = \begin{cases} 1 & \text{if } \mathcal{C}(\phi) \text{ encloses } \xi_R, \\ 0 & \text{otherwise.} \end{cases}$$

This is a nonuniform approximation in the sense indicated in §1.4.

The specularly reflected beam φ^g is given as

$$\varphi^g = AG(\phi)R(\phi)\,\frac{e^{\mathrm{i}kr}}{kr}. \qquad (2.16)$$

Using equations (1.18) and (1.19), and making approximations identical to those used to calculate (1.20), the leaky Rayleigh wave φ^R is given as

$$\varphi^R = -AG(\beta_R)\left(\frac{2\pi}{kr_R}\right)^{1/2} 2\alpha_R\, e^{\mathrm{i}\pi/4}\, e^{\mathrm{i}kr\cos(\xi_R - \phi)} \qquad (2.17)$$

where $r_R = \rho/\sin\beta_R$. The leaky Rayleigh-wave pole is defined by (1.18). The approximation (1.19) and the approximation $\xi_R \approx \beta_R$ have been used in the amplitude. The phase term can be expanded into real and imaginary parts to exhibit the fact that (2.17) is a leaky Rayleigh wave.

Equations (2.15)–(2.17) describe a scattered wavefield that consists of a diverging spherical wave emerging from $r = 0$, and a leaky Rayleigh wave

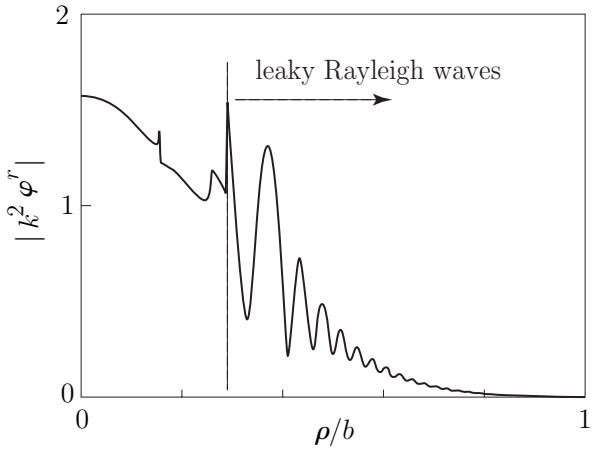

Figure 2.4: A plot of the magnitude of $|k^2\varphi^r|$ against ρ/b. Note the presence of the leaky Rayleigh wave, starting at $\rho/b \approx 0.3$, in the wavefield filling the aperture. Compare this figure with the solid curve in figure 2.3.

that is radiating from the interface. Both these waves are collected by the aperture and transmitted to the transducer. Figure 2.4 shows $|k^2\varphi^r|$ as a function of the scaled radius ρ/b, at $x_3 = -f$, the plane of the lens' aperture. The spikes in the graph arise from the fact that the asymptotic approximation is not uniform. The oscillations to the right of the large spike indicates the presence of the leaky Rayleigh wave in the aperture. It is important to note that the transducer responds to this entire signal; it does not sense or separate the individual parts.

The various parameter values used in Figure 2.4 are the following:

$$\begin{gathered}\rho_s = 2200\,\mathrm{kg/m^3},\ \ c_L = 5960\,\mathrm{m}/s,\ \ c_T = 3760\,\mathrm{m}/s,\\ \rho_f = 998\,\mathrm{kg/m^3},\ \ c = 1480\,\mathrm{m}/s,\\ F = 0.75,\ \ N = 178,\ \ n = 1,\ \ a/b = 0.5.\end{gathered} \tag{2.18}$$

The first line lists the parameter describing the solid, and the second those describing the coupling fluid; the solid is fused quartz and the fluid water. The third line list the parameters describing the lens and aperture. The frequency of operation is taken as 225 MHz. The leaky Rayleigh pole ξ_R is found numerically. The value of z_s is chosen such that $kz_s/2\pi = -10$. The constant A is given the same value as that used in Figure 2.3.

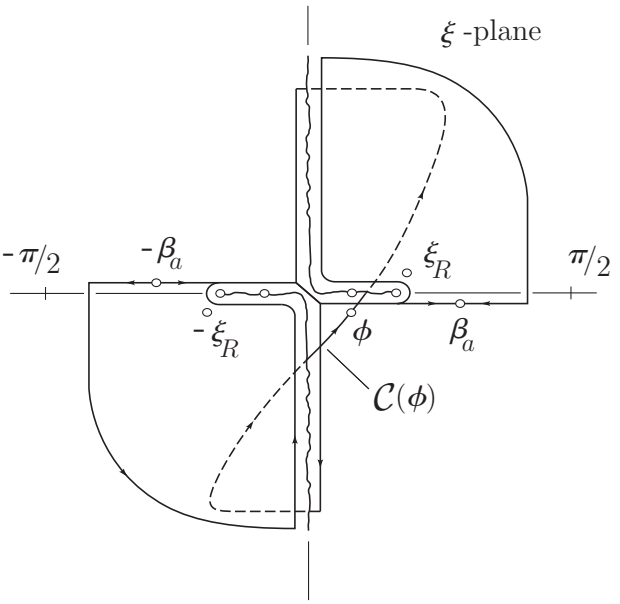

Figure 2.5: A sketch of the steepest descents contour for the case where $2z_s > x_3 > z_s$. The branch cut for $H_0^{(2)}$ is not shown. The somewhat complicated path is necessary because the integration contour can be closed at infinity only in the indicated quadrants.

2.5.3 Converging reflected beam, $2z_s < x_3 < z_s$

To approximate asymptotically the converging beam, where $2z_s < x_3 < z_s$, (2.7) is again used. The spherical coordinates (r, ϕ, θ) are introduced with $\phi \in [0, \pi/2)$. The contour in ξ is distorted to the contour $\Re[\cos(\xi - \phi)] = 1$ with no approximation of $H_0^{(2)}$ being made. This will become the contour of steepest descents. Figure 2.4 shows the complete distortion of the original contour into this contour. The branch cut for the $H_0^{(2)}$ is not shown. The dashed lines indicate that the contour must be distorted onto a lower Riemann sheet in order for the contour to pass through the stationary point $\xi = \phi$. This means that branch cuts are surrounded; however, these contributions are ignored. The pole terms are now extracted giving

$$\varphi^R = -\mathrm{i}\, 2\pi A\, G(\beta_R)\, \alpha_R \sin\beta_R\, e^{-\mathrm{i}kr\cos\phi\cos\xi_R} \times \left[H_0^{(1)}(k\rho\sin\xi_R) - \chi_c(\xi_R,\phi) H_0^{(2)}(k\rho\sin\xi_R)\right] \quad (2.19)$$

where

$$\chi_c(\xi_R,\phi) = \begin{cases} 1 & \text{if } \mathcal{C}(\phi) \text{ encloses } \xi_R, \\ 0 & \text{otherwise,} \end{cases}$$

and $\rho = r\cos\phi$. The leaky Rayleigh-wave pole is given by (1.18). The approximation (1.19) and the approximation $\xi_R \approx \beta_R$ have been used in the amplitude. Note that the indicator $\chi_c(\xi_R, \phi)$ sets the second term to zero when ϕ is greater than β_R, whereas $\chi_d(\xi_R, \phi)$ sets the corresponding term in (2.15) to zero when ϕ is less than β_R. When ϕ is less then β_R both Hankel functions are present indicating that the leaky Rayleigh waves are focusing on the interface and along the axis $\rho = 0$. Moreover, the first Hankel function is always present because the pole $-\xi_R$ is always captured. When ϕ is greater then β_R this term represents an outgoing, cylindrical, leaky Rayleigh wave. Writing the pole terms as Hankel functions gives an expression that is accurate when $\rho \to 0$.

Once the pole terms have been extracted, the remaining integral can be approximated by introducing the asymptotic approximation to $H_0^{(2)}$, and noting that the contour of integration is that of steepest descents. The geometrical term is approximated as

$$\varphi^g \sim -AG(\phi)R(\phi)\,\frac{e^{-\mathrm{i}kr}}{kr}. \quad (2.20)$$

This expression is accurate when $2z_s < x_3 < z_s$, provided $z_s \neq 0$, or equivalently $r \neq 0$. Note the phase shift of π in passing from (2.20) to (2.16).

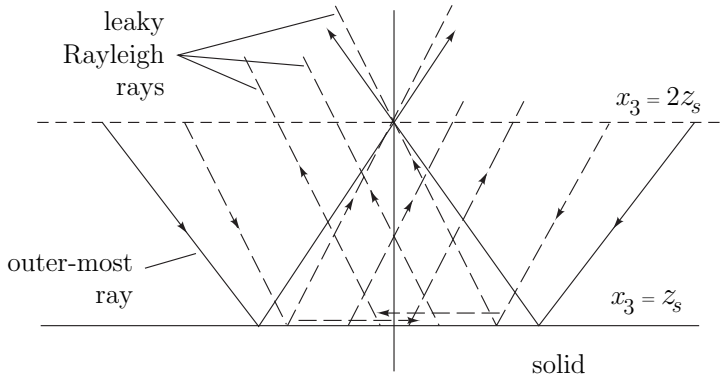

Figure 2.6: A sketch of the rays describing the focusing scattered beam. The solid lines indicate the outermost geometrical rays, and the dashed ones the leaky Rayleigh waves.

The asymptotic approximation to φ^r is therefore given as

$$\varphi^r \sim \varphi^g + \varphi^R, \quad kb \to \infty, \tag{2.21}$$

where φ^R is given by (2.19), with no restriction on ρ, and φ^g by (2.20), with the restriction that $r \neq 0$. Accordingly, the overall expression is only accurate provided the reflected focal plane and the interface are separated. Moreover, (2.21) is a nonuniform approximation in the sense indicated in §1.4. While (2.21) is limited in its usefulness, it does provide a good physical picture of what is happening. Figure 2.6 is a sketch that attempts to illustrate this equation. The solid lines indicate the outer most rays of the focused cone of rays: They reflect from the interface and are focused in the reflected focal plane. The dashed lines indicate the leaky Rayleigh waves: Within a right circular cone, which opens downward and ends at the interface, intersecting it to form a circle with radius $|z_s| \tan \beta_R$, they focus on the axis $\rho = 0$, whereas, outside the cone, they form an outgoing cylindrical wave steadily leaking into the coupling fluid.

2.6 Measurement model

The previous section describes the reflected focused beam and leaky surface wave, but does not indicate how that scattered wavefield is transformed into a change in voltage. Looking back at Figure 2.1(a), it is readily appreciated that the basic function of the lens, buffer rod and piezoelectric transducer is to map the total echo collected by the aperture of the lens to a change

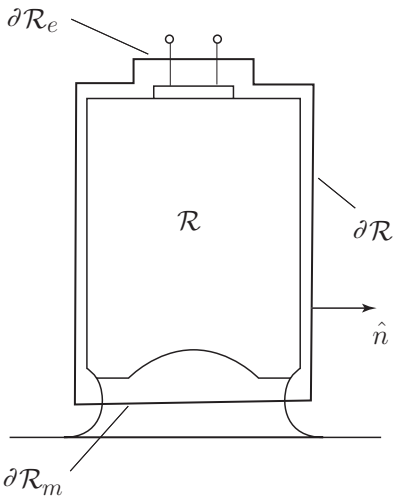

Figure 2.7: The volume $\mathcal{R}$ in which the reciprocity relation is applied. The surface $\partial\mathcal{R}$ includes the electrical plane $\partial\mathcal{R}_e$ and the mechanical plane $\partial\mathcal{R}_m$.

in voltage δV. To construct a mathematical model of this mapping the electromechanical reciprocity identity described in §A.4 and given by (A.8) is used. An early use of this identity to construct such models is given by Auld (1979). The outcomes from using it are often called *measurement models*. When no sources are present this identity becomes

$$\partial_i \left[-\mathrm{i}\omega(u_j^1 \tau_{ij}^2 - u_j^2 \tau_{ij}^1) + e_{ijk}(E_j^1 H_k^2 - E_j^2 H_k^1) \right] = 0. \tag{2.22}$$

To use (2.22) several assumption must be made: The electromechanical reciprocity identity holds throughout $\mathcal{R}$, whatever the internal structure of the real device. The wavefields on the surface $\partial\mathcal{R}$ are assumed to be such that all electromagnetic waves enter or leave $\mathcal{R}$ through the electrical plane $\partial\mathcal{R}_e$, and all mechanical waves enter or leave through the mechanical plane $\partial\mathcal{R}_m$; elsewhere on $\partial\mathcal{R}$ the wavefields vanish. The two planes are considered subsets of the overall surface $\partial\mathcal{R}$ and are identified in Figure 2.7.

The transducer is connected to the electrical source and receiver through a co-axial cable. Only a transverse, electromagnetic, plane wave propagates in a coaxial cable (Collin 1991, pp. 247–251); all higher modes are cut-off. By placing $\partial\mathcal{R}_e$ far enough from the junction of the co-axial cable with the transducer, it can be assumed that any higher modes that might be excited at the junction have become negligible; therefore, at $\partial\mathcal{R}_e$ only a transverse plane wave is present.

Lastly, it is assumed that the multiple scattering that occurs between the lens' aperture and the interface is negligible. This is a reasonable though imperfect assumption because tone-bursts, not time-harmonic signals, are used, and thus any multiply scattered signals can be separated, in time, from the first echo. The δV calculated in this chapter, which uses the time-harmonic assumption, is a Fourier transform of the change in voltage detected in time. At the mechanical plane $\partial\mathcal{R}_m$, therefore, it is assumed that the scattered disturbance has been scattered from the interface only once.

Equation (2.22) is integrated over the volume $\mathcal{R}$, shown in Figure 2.7, and transformed into a surface integral over $\partial\mathcal{R}$. This gives

$$\int_{\partial\mathcal{R}_e} e_{ijk}(E_j^1 H_k^2 - E_j^2 H_k^1) n_i \, dS = \mathrm{i}\omega \int_{\partial\mathcal{R}_m} (u_j^1 \tau_{ij}^2 - u_j^2 \tau_{ij}^1) n_i \, dS. \tag{2.23}$$

Wavefield 1 is taken as

$$E_i^1 = (1 + R_e) E_i^+, \;\; H_i^1 = (1 - R_e) H_i^+, \;\; u_j^1 = u_j^i, \;\; \tau_{ij}^1 = -p^i \delta_{ij}. \tag{2.24}$$

The first two terms are assumed to be evaluated at $\partial\mathcal{R}_e$, and the last two at $\partial\mathcal{R}_m$. This is the wavefield that is present when there is no interface. The first two terms describe the transverse electromagnetic wave in the co-axial cable; there is both an incident and reflected term, the reflection arising from the junction between the cable and transducer. In practise the designer tries to make R_e as small as possible. The second two terms describe the focused sound beam that is radiated from the lens' aperture. Wavefield 2 is taken as

$$\begin{gathered} E_i^2 = (1 + R_e + \delta R_e) E_i^+, \;\; H_i^2 = (1 - R_e - \delta R_e) H_i^+, \\ u_j^2 = u_j^i + u_j^r, \;\; \tau_{ij}^2 = -(p^i + p^r) \delta_{ij}. \end{gathered} \tag{2.25}$$

As with (2.24), the first two terms are assumed to be evaluated at $\partial\mathcal{R}_e$, and the last two at $\partial\mathcal{R}_m$. This is the wavefield that is present when sound is scattered back to the lens' aperture from the interface. The first two terms again describe the transverse electromagnetic wave in the co-axial cable; there is now an increment to the reflection, δR, arising from the sound collected at the aperture. The second two terms describe a focused sound beam that is incident to and scattered from the interface. Substituting equations (2.24) and (2.25) into (2.23) gives

$$\delta R_e = \frac{\mathrm{i}\omega}{4\,P} \int_{\partial\mathcal{R}_m} (u_j^r p^i - u_j^i p^r) n_j \, dS, \tag{2.26}$$

where

$$P = -\frac{1}{2}\int_{\partial\mathcal{R}_e} e_{ijk} E_j^+ H_k^+ n_i \, dS.$$

The normalization P is the incident power injected into the junction of the cable with the transducer, so that it is known.

Despite the assumptions leading to it, (2.26) is quite remarkable for at least two reasons. First it maps the mechanical wavefield at $\partial\mathcal{R}_m$ to what is measured at the electrical plane $\partial\mathcal{R}_e$. Note that it clearly indicates how the transducer responds only to the complete signal, returning a single scalar quantity δR_e. Secondly, the incident focused beam has a limited angular spectrum because the aperture is finite; thus its combination with scattered wavefields explicitly limits the angular spectrum of the scattered wavefield that can be collected.

2.7 Acoustic material signature

Because the incident and reflected wavefields in the coupling fluid have been expressed in terms of potentials, it is convenient to express (2.26) in terms of them as well. From §A.2,

$$p^{i,r} = \rho_f \omega^2 \varphi^{i,r}, \quad u_i^{i,r} = \partial_i \varphi^{i,r}.$$

It is also convenient to renormalize (2.26) so that its maximum absolute value is approximately one. The plane $\partial\mathcal{R}_m$ is taken to be the interface $x_3 = z_s$. The outcome is an expression for a term labeled δV which is proportional to δR_e. δV is named the change in voltage, though it is dimensionless, because it is proportional to the change in measured voltage caused by the presence of the interface and any features on it. The δV is given as

$$\delta V = E \int_{\partial\mathcal{R}_m} (\partial_n \varphi^i \, \varphi^s - \varphi^i \, \partial_n \varphi^s) \, dS, \tag{2.27}$$

where

$$E^{-1} = 2 \int_{\partial\mathcal{R}_m} (\partial_n \varphi^i \, \varphi^{i\,*}) \, dS.$$

Equations (2.6) and (2.12) indicate that the incident and reflected wavefields are inverse Hankel transforms. Examining (2.27) it becomes clear that it is an integral of the product of Hankel transforms over a semi-infinite domain. This permits the Parseval's relation, given in §4.5 by (A.10), to be used to collapse what might seem to be a complicated triple integral into a

single one. This is a key step in the derivation, but not one that could be foreseen when the work was first begun. Carrying out this step gives

$$\delta V(\mathbf{s}, z_s) = 2\mathrm{i}D \int_0^{\beta_a} G^2(\xi)\, R(\xi, \mathbf{s}) e^{\mathrm{i}2kz_s \cos\xi}\, d\xi, \tag{2.28}$$

where $D = k^5 E$ or

$$D^{-1} = 2\mathrm{i} \int_0^{\beta_a} G^2(\xi) \sin\xi d\xi.$$

This is the central result of this chapter. A dependence on the position on the interface is indicated by $\mathbf{s}$, and a dependence on the position of the geometric focal plane by z_s. If $z_s \approx 0$ then (2.28) describes how the reflection acoustic microscope makes an image when it is scanned across the interface. In this case no leaky Rayleigh wave is excited. Assuming that $R(\xi, \mathbf{s})$, as a function of $\mathbf{s}$, changes slowly with respect to wavelength — this is equivalent to assuming that no vertical discontinuities are present — then (2.28) maps the reflection at $\mathbf{s}$ to a change in voltage at the same position. The set of all these reflections, when converted to electrical signals, is the image. Note that δV is a weighted average over the lens aperture of the reflection coefficient; the weight function is the square of the aperture function $G(\xi)$. In other words, perfect information about the interface is not recovered.

When $\mathbf{s}$ is fixed and z_s varied the acoustic microscope acts as an interferometer. A nonuniform asymptotic approximation of (2.28), for $|z_s| \neq 0$, gives

$$\begin{aligned}\delta V(\mathbf{s}, z_s) \sim \pm DG^2(0)\, R(0, \mathbf{s})\, \frac{e^{\mathrm{i}2kz_s}}{k|z_s|} \\ - H(-z_s)\, DG^2(\beta_R)\, 8\pi\mathrm{i}\, \alpha_R \sin\beta_R\, e^{-2\mathrm{i}k|z_s|\cos\xi_R}, \\ z_s \gtrless 0, \;\; kb \to \infty.\end{aligned} \tag{2.29}$$

$H(x)$ is the Heaviside step function. Note that no leaky Rayleigh wave is collected by the lens' aperture for $z_s > 0$. The approximations (1.19) and $\xi_R \approx \beta_R$ have been used in the amplitude, in the second term.

For z_s negative (2.29) indicates that δV records an interference pattern as z_s is varied. Figure 2.8 shows a plot of this interference pattern for fused quartz. The values are identical to those used for Figure 2.4 and are cited in (2.18). The solid line indicates the asymptotic result (2.29), and the dashed line a numerical evaluation of (2.28). The interference pattern is evident. The distance between the peaks Δ is given by the equation

$$\Delta = 2(1 - \cos\beta_R)^{-1}$$

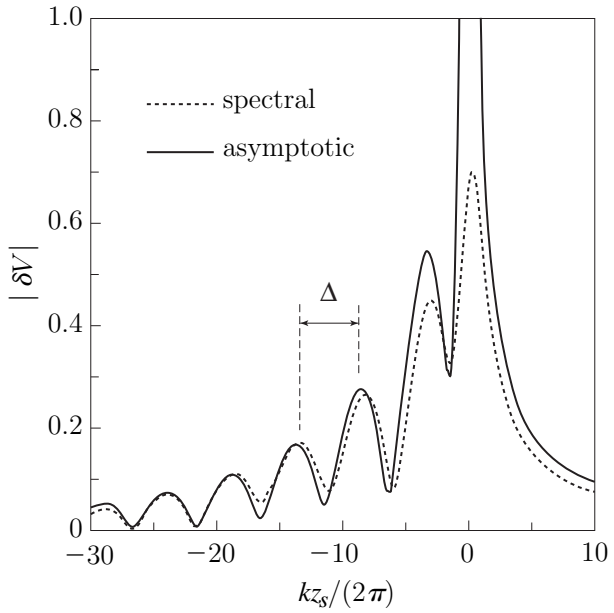

Figure 2.8: The acoustic material signature of fused quartz. The solid line indicates the result of plotting the asymptotic approximation, and the dashed line indicates a numerical evaluation of (2.28). Δ is the distance between the peaks.

From this the variation in the Rayleigh wavespeed can be determined. The graph shown in Figure 2.8 is named the *acoustic material signature*.

Much more can be done with (2.28). If the geometrical focal plane is placed just slightly below the interface, the leaky Rayleigh wave participates in the image formation causing vertical surface features, such as the opening of a surface-breaking crack, to be detected acoustically, even when they are difficult to detect with an optical microscope. The monograph by Briggs (1992) gives many examples of this feature. Rebinsky and Harris (1992b) show that the leaky surface wave can be used to set up an interference pattern between the incident surface wave and one reflected from a vertical discontinuity. Lastly, (2.28) is a more general imaging expression than its derivation might suggest. Many scanning, acoustic detection schemes used in industrial nondestructive evaluation work more or less in the same manner as does a reflection acoustic microscope so that (2.28) or a minor modification of it describes a wide variety of such schemes.

2.8 Summary

1. Equations (2.5) and (2.10) describe a model of a focused beam. It does not exactly describe focusing through an aperture, as a study of focusing calculations that begin at the plane of the aperture indicate (Born and Wolf 1999, pp. 484–499), but its form allows one to readily calculate the scattering of a focused beam, and, just as importantly, invoke a Parseval's relation to calculate δV.

2. Equation (2.11) and the analysis of §2.5 describe the reflected focused beam. Of particular interest is the fact that the leaky Rayleigh waves form a second focal point at the interface. Though not discussed in this chapter, this feature is important in detecting small surface features such as the opening of a surface-breaking crack (Rebinsky and Harris 1992b; Rebinsky and Harris 1992a).

3. The discussion of §1.6 leading to (2.26) indicates how one may relate the measured electrical signal from a piezoelectric transducer to the scattered mechanical wavefields, and as such this plays an important role in many elastodynamic measurement models.

4. Equation (2.28) is the principal result of this chapter. It is the equation that describes how a reflection acoustic microscope makes an image and acts as an interferometer. In one guise or another it describes acoustic imaging in many other situations that arise in the nondestructive evaluation of manufactured parts.

Chapter 3

Coupled, local elastodynamic modes

Abstract

The coupling of the two lowest Rayleigh-Lamb modes, guided within a homogeneous layer, but perturbed by the presence of a slowly varying change in thickness, is described using the coupled, local mode approximation. By projecting the elastic-wave equations onto a basis of local eigenmodes, an infinite system of coupled-mode equations describing the evolution of the amplitudes of each mode is obtained. Within the equations, the coupling is manifested by coupling coefficients that depend critically on the difference between the wavenumbers of adjacent modes. At high frequencies the wavenumbers of the two lowest Rayleigh-Lamb modes approach one another, and both approach the wavenumber describing a Rayleigh wave. Hence, the surface perturbation causes the two lowest modes to couple, forming a modulated Rayleigh surface-wave, if propagating from a thinner to a thicker section; or a Rayleigh surface-wave to split apart forming two separate modes, if propagating in the opposite sense. In contrast, both modes couple only weakly to the higher-order modes, because their wavenumbers do not approach those of the higher modes for any frequencies.

3.1 Introduction

The interaction of guided surface-waves with surface irregularities plays an important role in enhancing the acoustic images of such features, as indicated in Chapter 2. While the problem described here does not apply directly to imaging, it is a beginning of an effort toward obtaining analytic expressions describing scattering by surface irregularities. Such expressions would then be incorporated into the measurement model (2.26), or into the imaging equation (2.28), to give a more comprehensive theory of the image formation

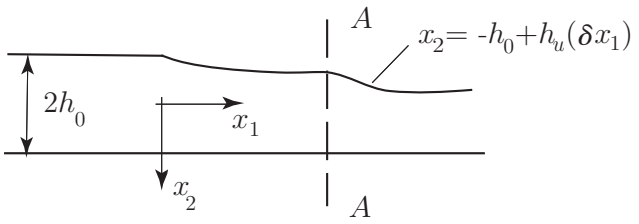

Figure 3.1: The geometry of the elastic layer with variable thickness. The variable surface is described by $h_u(\delta x_1)$. The two lowest Rayleigh-Lamb modes are assumed to be excited in the uniform region at the left, and are propagating to the right. The coordinates and lengths shown are dimensionless: the scaling is described in §3.1.2. Note that the coordinate x_2 is now measured down the page, in contrast to the convention of the previous chapters.

of these features. This is the principal motivation for studying this problem.

3.1.1 Description of the problem

Figure 3.1 sketches a homogeneous, isotropic, elastic layer with a variable thickness described by the curve $x_2 = -h_0 + h_u(\delta x_1)$, where δ is a small parameter determining the rate of change of the thickness. The nominal thickness is $2h_0$. The problem considered in this chapter is the following: The two lowest Rayleigh-Lamb modes are excited in the uniform region of the layer shown in Figure 3.1, and are incident to the nonuniform region, at the right. What then is the effect of the variable change in thickness on the propagation of these two modes?

Rayleigh-Lamb modes are described in several books: Achenbach (1973, pp. 220–236), Auld (1990a, pp. 76–94), Brekhovskikh and Goncharov (1985, pp. 75–86), and Miklowitz (1978, pp. 178–209). They are in-plane elastic waves that are guided in a uniform, two-dimensional waveguide with traction-free surfaces. The equations describing two-dimensional, in-plane, elastic waves are obtained from (A.1) – (A.3) by setting u_3 and all derivatives ∂_3 to zero; that is, the only particle displacement occurs in the (x_1, x_2)-plane and the independent spatial variables are (x_1, x_2).

Figure 3.2 shows a sketch of the dispersion relations for the two lowest Rayleigh-Lamb modes in a layer of uniform thickness $2h_0$. Note that at large h_0 the wavespeeds of both these modes approximate that of the Rayleigh wavespeed, the line labeled c_R; in §3.2 it is shown that, these two modes

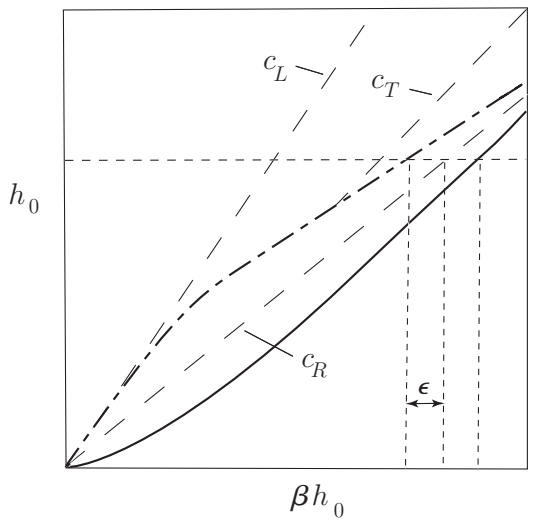

Figure 3.2: A sketch of the dispersion relation for the two lowest Rayleigh-Lamb modes. Recall that $h_0 = \omega H_0/c_T$. Solid curve: antisymmetric mode, eigenvalue $\beta_a = \beta_R + \epsilon_a$. Short-dash, long-dash curve: symmetric mode, eigenvalue $\beta_s = \beta_R - \epsilon_s$. $\epsilon_a + \epsilon_s = 2\epsilon$ measures the horizontal distance between the two curves. At large h_0, $\epsilon_a = \epsilon_s = \epsilon$, where $\epsilon \ll 1$, as indicated in the figure. c_L, c_T and c_R are the compressional, shear and Rayleigh wavespeeds; the long-dashed lines indicate the slopes c_L/c_T, 1, and c_R/c_T.

combine to form a modulated Rayleigh surface-wave. At large h_0 all the remaining modes approach the line labeled c_T. If the uniform region of the layer, in Figure 3.1, is thicker than that at the right, then h_0 is imagined to be in the range where the two lowest Rayleigh-Lamb modes approximate a Rayleigh surface-wave on the upper surface. If the uniform region is thinner, then it is imagined that the region on the right grows to a thickness such that the two lowest modes gradually coalesce to form a Rayleigh surface-wave on the upper surface (this case is not shown in Figure 3.1). Therefore the problem being studied is asking either how a Rayleigh surface-wave is split into the two lowest Rayleigh-Lamb modes, or how these two modes couple to form a Rayleigh surface-wave.

It is important to note that the two lowest Rayleigh-Lamb modes have different symmetries and are governed by different dispersion relations (see §3.2). The coupling is therefore not that of two modes which are themselves coalescing; that is, the wavenumbers coalesce, but the particle displacements, as functions of x_2, remain distinct. This should be contrasted with the case where the modes themselves coalesce as their wavenumbers do. Such modes are said to become degenerate (Budden and Eve 1975). This latter case causes critical coupling and has been studied by Budden (1975).

3.1.2 Background

A variation of this problem was studied previously, by Folguera and Harris (1999), by calculating a WKBJ approximation to each lowest mode *separately* and then adding the two expressions to calculate the composite disturbance. However, the higher-order terms in this approximation contained a term that depended inversely on the difference between the wavenumber of the lowest mode being considered and that of the other lowest mode. A difficulty then arises because these higher-order terms can become very large as the wavenumbers both approach the Rayleigh wavenumber, and hence one another, at high frequencies. At the time, the difficulty was noted, but no solution given. The present description, using coupled modes, resolves this.

The basic idea underlying the coupled, local mode approximation is the following: The wavefields at any cross-section, such as A–A in Figure 3.1, are expanded in those modes that would propagate in a guide having parallel faces and the thicknesses of section A–A. This is what is meant by the adjective local. Subsequently, by using the orthogonality relation for the eigenmodes, a system of evolution equations in x_1 for the coefficients

multiplying each eigenmode is derived. This technique has been used to study sound (Brekhovskikh and Godin 1999, pp. 244–282, 429–446) and electromagnetic propagation (Shevchenko 1971) in inhomogeneous waveguides. And, by Kennett (1984), as prelude to using invariant embedding to calculate global transmission and reflection coefficients from a section of inhomogeneity in an otherwise uniform waveguide.

The WKBJ approximation has itself been extensively studied. The monographs Jeffreys (1962) and Heading (1962), and the review article Berry and Mount (1972) discuss such approximations for second-order differential equations with an emphasis on the impact of turning points of various kinds on the approximate solutions. WKBJ solutions to systems of equations are explained by Wasow (1987) and Fedoryuk (1993); application of these matrix WKBJ methods to waves in elastic shells is described by Steele (1976).

3.1.3 Notation

The wavenumber $k_T = \omega/c_T$ and is used, initially, to scale lengths; ω is the angular frequency and c_T is the shear wavespeed. The Rayleigh wavespeed c_R is approximately $0.9c_T$, so that at high frequencies the shear-wave wavelength approximates the Rayleigh-wave wavelength. Upper case letters represent the unscaled lengths and lower case letters the scaled ones, unless otherwise indicated. The coordinates are $x_\alpha = k_T X_\alpha$; the particle displacement components are $u_\alpha = k_T U_\alpha$; the nominal thickness of the guide is $2h_0 = 2k_T H_0$.

The shear coefficient μ is used to scale the stress components: $\tau_1 = \tau_{11}/\mu, \tau_2 = \tau_{12}/\mu$ and $\tau_3 = \tau_{22}/\mu$, where the $\tau_{\alpha\beta}$ are the unscaled components. The subscripts $\alpha, \beta = 1, 2$. *Note*: This is the only place in this chapter where two subscripts are needed; elsewhere, $\tau_{p\,\alpha}$ indicates the pth mode, the α component.

It is useful to introduce combinations of elastic parameters that will arise frequently. These are:

$$a = \lambda/(\lambda + 2\mu), \quad b = \mu/(\lambda + 2\mu), \quad c = 4(a + b). \tag{3.1}$$

Also of use is the relation

$$\tau_3 = a\tau_1 + c\,\partial_2 u_2. \tag{3.2}$$

3.2 Rayleigh-Lamb modes

The two lowest Rayleigh-Lamb modes are given by the following expressions, which are taken from Brekhovskikh and Goncharov (1985, pp. 75–86). These are local modes in the sense described previously, so that some of their parameters change with δx_1 to accommodate the change in thickness. The lowest antisymmetric mode $\mathbf{u}_a$ is given as

$$\begin{bmatrix} u_{a\,1}(\delta x_1, x_2) \\ \\ u_{a\,2}(\delta x_1, x_2) \end{bmatrix} = C_a \begin{bmatrix} \dfrac{\sinh(\gamma_L \bar{x}_2)}{\cosh(\gamma_L \bar{h}_0)} - \dfrac{\gamma_L\,\gamma_T}{p\beta_a} \dfrac{\sinh(\gamma_T \bar{x}_2)}{\cosh(\gamma_T \bar{h}_0)} \\ \\ \dfrac{-\mathrm{i}\gamma_L}{\beta_a} \left[\dfrac{\cosh(\gamma_L \bar{x}_2)}{\cosh(\gamma_L \bar{h}_0)} - \dfrac{\beta_a}{p} \dfrac{\cosh(\gamma_T \bar{x}_2)}{\cosh(\gamma_T \bar{h}_0)} \right] \end{bmatrix}, \tag{3.3}$$

while the lowest symmetric mode $\mathbf{u}_s$ is given as

$$\begin{bmatrix} u_{s\,1}(\delta x_1, x_2) \\ \\ u_{s\,2}(\delta x_1, x_2) \end{bmatrix} = C_s \begin{bmatrix} \dfrac{\cosh(\gamma_L \bar{x}_2)}{\sinh(\gamma_L \bar{h}_0)} - \dfrac{\gamma_L\,\gamma_T}{p\beta_s} \dfrac{\cosh(\gamma_T \bar{x}_2)}{\sinh(\gamma_T \bar{h}_0)} \\ \\ \dfrac{-\mathrm{i}\gamma_L}{\beta_s} \left[\dfrac{\sinh(\gamma_L \bar{x}_2)}{\sinh(\gamma_L \bar{h}_0)} - \dfrac{\beta_s}{p} \dfrac{\sinh(\gamma_T \bar{x}_2}{\sinh(\gamma_T \bar{h}_0)} \right] \end{bmatrix}. \tag{3.4}$$

In (3.3) β_a is substituted wherever needed; in (3.4) β_s is substituted wherever needed. C_a and C_s are arbitrary constants.

The equations whose solutions give the dispersion relation for each mode are

$$\gamma_L \gamma_T \tanh(\gamma_{T,L}\, \bar{h}_0) = p^2 \tanh(\gamma_{L,T}\, \bar{h}_0), \tag{3.5}$$

where the first subscript gives the antisymmetric relation and the second the symmetric one. The radicals γ_L and γ_T are defined as

$$\gamma_L = (\kappa^2 \beta^2 - 1)^{1/2}/\kappa, \quad \gamma_T = (\beta^2 - 1)^{1/2}, \quad \kappa = c_L/c_T = a^{-1/2},$$

where c_L is the compressional wavespeed. As Figure 3.2 suggests, $\gamma_{L,T}$ are real and positive. The term p is defined as

$$p = (\beta^2 - 1/2)/\beta.$$

The coordinate $\bar{x}_2$ and half-thickness $\bar{h}_0$ are given by

$$\bar{x}_2(\delta x_1) = x_2 - [h_u(\delta x_1)/2], \quad \bar{h}_0(\delta x_1) = [2h_0 - h_u(\delta x_1)]/2.$$

These transformations move the local coordinate system so that, at A–A in Figure 3.1, $\bar{x}_2 = 0$ at the local centerline, and $2\bar{h}_0$ is the local thickness.

Note: This is where the δx_1 dependence enters. It enters not only explicitly through these expressions, but also implicitly through the $\beta_{a,\,s}$; these solutions to the antisymmetric and symmetric dispersion equations, (3.5), depend on $\bar{h}_0$.

It is useful to express $\beta_{a,\,s}$ as

$$\beta_a = \beta_R + \epsilon_a, \quad \beta_s = \beta_R - \epsilon_s, \quad \epsilon_a + \epsilon_s = 2\epsilon \tag{3.6}$$

where β_R is the wavenumber of a Rayleigh surface wave, and $2\epsilon = (\beta_a - \beta_s)$. In general, ϵ is not small and must be found from a knowledge of $\beta_{a,\,s}$. However, as Figure 3.2 suggests, as $\bar{h}_0$ (or more simply h_0) becomes large, $\epsilon_a \to \epsilon_s \to \epsilon$, and ϵ is given by

$$\epsilon(\delta x_1) = 2p^2 \left(e^{-2\gamma_L \bar{h}_0} - e^{-2\gamma_T \bar{h}_0}\right) \left(\frac{df_R}{d\beta}\right)^{-1}. \tag{3.7}$$

This approximation is taken from Brekhovskikh and Goncharov (1985, pp. 79–81). β_R is used wherever β is needed. The approximation (3.7) is accurate provided $\gamma_T \bar{h}_0 > 1$, or, more approximately stated, provided $\bar{h}_0 \gg 1$. The Rayleigh function, given as

$$f_R(\beta) = p^2 - \gamma_L\, \gamma_T,$$

has roots $\pm\beta_R$. The Rayleigh wavenumber β_R is approximated (Auld 1990a, p. 92) by

$$\beta_R = \omega / c_R, \quad \frac{c_R}{c_T} = \frac{(0.87 + 1.14\nu)}{1 + \nu},$$

where $\nu = \lambda / \left[2(\lambda + \mu)\right]$.

For a uniform guide, ϵ_a and ϵ_s are constant, $\bar{x}_2 = x_2$ and $\bar{h}_0 = h_0$. Therefore, the sum of these two modes gives the net particle displacement

$$\mathbf{U} = e^{\mathrm{i}\beta_R x_1}\, C\, \left(e^{\mathrm{i}\epsilon_a x_1} \mathbf{u}_a + e^{-\mathrm{i}\epsilon_s x_1} \mathbf{u}_s\right), \tag{3.8}$$

where $C_a = C_s = C$. *At large* h_0, it is very difficult to excite just one mode because $\epsilon_{a,\,s} \approx \epsilon \ll 1$. Hence, even for a uniform guide, both modes would be excited. Once excited, however, both modes *propagate independently*. Equation (3.8) becomes a wave propagating at the Rayleigh wavespeed, but with a modulated amplitude. Approximating (3.3) and (3.4) for large h_0 would indicate that (3.8) has most of its amplitude near the upper surface and decays towards $x_2 = 0$; its amplitude near the lower surface is negligible. It is effectively a Rayleigh wave. When the term Rayleigh surface-wave was used

in §3.1.1, this was the wave being referred to. If the propagation path is long enough the two terms will move out of phase so that the Rayleigh wave will shift from the upper surface to the lower one, (Auld 1990a, pp. 93,94) and (Brekhovskikh and Goncharov 1985, pp. 79–81). Experimental confirmation of this shifting is described by Ti, O'Brien, and Harris (1997).

3.3 Coupled, local mode approximation

The general theory of coupled, local modes, in a form that differs from that which follows, is described by Maupin (1988), and, in particular, her idea of using an equivalent body force to take account of the sloping boundary is used here. The difficulty with capturing the effect of a sloping boundary in coupled-mode calculations was previously noted by Rutherford and Hawker (1981) in the context of underwater acoustics.

3.3.1 A framework for elastic waveguide problems

The equations of motion will be written in a form that is not found in the books cited in §1.1.1, though it is used by Harris and Block (2005), Kirrmann (1995), and Maupin (1988). This manner of writing the equations of motion was also used for antiplane shear problems by Malischewsky (1987, pp. 54–69). The purpose of finding an alternative way of writing the equations of motion, (A.1)–(A.3), is to eliminate second-order derivatives of the form $\partial_1 \partial_2$ so that, when the pth eigenmode is sought, the eigenvalue β_p will appear in an isolated way.

The vector

$$\mathbf{U} := [u_1, u_2, \tau_1, \tau_2]^T$$

is introduced, where, the superscript T indicates the transpose. The equations of motion are then written as

$$(\mathcal{L} - \partial_1)\,\mathbf{U} = \mathbf{F}, \tag{3.9}$$

where

$$\mathcal{L} := \begin{bmatrix} 0 & -a\,\partial_2 & b & 0 \\ -\partial_2 & 0 & 0 & 1 \\ -1 & 0 & 0 & -\partial_2 \\ 0 & -c\,\partial_2^2 - 1 & -a\,\partial_2 & 0 \end{bmatrix}. \tag{3.10}$$

$\mathbf{F}$ is a vector containing body forces and is described by

$$\mathbf{F} = [0, 0, f_1, f_2]^T,$$

where the $f_\alpha = F_\alpha/(k_T\mu)$. The F_α are the unscaled body-force components per unit mass. The constants a, b and c are given by (3.1). This system of equations is derived by using both the equation of motion (A.1) and the constitutive relation (A.2), and subsequently using (3.2) to eliminate τ_3 from the equations.

An inner product is defined as

$$\langle \mathbf{V}, \mathbf{U} \rangle := -\mathrm{i} \int_{-h_0+h_u(\delta x_1)}^{h_0} \left(v_\beta^* \tau_\beta - \sigma_\alpha^* u_\alpha \right) dx_2, \tag{3.11}$$

where

$$\mathbf{V} = [v_1, v_2, \sigma_1, \sigma_2]^T, \quad \mathbf{U} = [u_1, u_2, \tau_1, \tau_2]^T.$$

Using this inner product, the following integration by parts relation is calculated:

$$\langle \mathcal{L}\mathbf{V}, \mathbf{U} \rangle + \langle \mathbf{V}, \mathcal{L}\mathbf{U} \rangle = \mathrm{i} \left[(v_1^* \tau_2 - \sigma_2^* u_1) + (v_2^* \tau_3 - \sigma_3^* u_2) \right] \Big|_{-h_0+h_u(\delta x_1)}^{h_0}. \tag{3.12}$$

τ_3 is given by (3.2) and σ_3 is defined similarly.

For the moment, imagine that the guide is uniform with a thickness $2\bar{h}_0$. Consider a wave of the form

$$\mathbf{U} = \mathbf{u}_p(x_2) e^{\mathrm{i}\beta_p x_1}.$$

Substituting this into (3.9), with $\mathbf{F}$ set to zero, gives the following eigenvalue problem:

$$\begin{gathered} \mathcal{L}\mathbf{u}_p = \mathrm{i}\beta_p \mathbf{u}_p, \\ \tau_{p\,2} = \tau_{p\,3} = 0, \text{ at } x_2 = -h_0 + h_u(\delta x_1),\ x_2 = h_0, \end{gathered} \tag{3.13}$$

where the x_1 is fixed. $\mathbf{u}_p$ is the eigenmode and β_p the eigenvalue.

The eigenmodes of (3.13) are numbered as follows: They occur in pairs and are labelled so that one member of each pair carries energy or decays exponentially in the $+x_1$ direction, while the other member does so in the $-x_1$ direction. Subscripts p are integers and take plus and minus values, but not 0; a plus value is taken for propagation in the $+x_1$ direction and a minus is taken for propagation in the $-x_1$ direction. Thus $\beta_{-p} = -\beta_p$. Equations (3.3) and (3.4) are two eigenmodes that satisfy (3.13). However, they have different symmetries; $\beta_1 = \beta_a$ satisfies the antisymmetric dispersion equation, while $\beta_2 = \beta_s$ the symmetric dispersion equation; both dispersion equations are given by (3.5). In the development of this section subscripts $1, 2, \ldots$ will be used to identify the eigenvalues β_p with no indication of the symmetry.

Consider next two eigenmodes $\mathbf{u}_p$ and $\mathbf{u}_q$. Substituting them into (3.12) gives

$$-\mathrm{i}(\beta_q^* - \beta_p)P_{qp} = 0, \quad P_{qp} := \langle \mathbf{u}_q, \mathbf{u}_p \rangle. \tag{3.14}$$

This is the orthogonality condition. Note that the eigenvalues can be complex, though in practise the two eigenvalues of interest $\beta_{a,s}$ are always real.

A more precise description of the previous expressions is to state that the eigenmodes form a biorthogonal system, that $-\mathcal{L}$, with the same boundary conditions as indicted in (3.13), is the adjoint operator, and that (3.14) is an expression of biorthogonality. It is assumed throughout this chapter that the $\mathbf{u}_p(x_2)$ form a complete set, and thus a vector $\mathbf{U}(x_2)$ can be uniquely expressed as

$$\mathbf{U}(x_2) = \sum_n c_n \mathbf{u}_n(x_2).$$

These issues are discussed further by Kirrmann (1995) and Besserer and Malischewsky (2004). And a general discussion of biorthogonal expansions is given by Herrara and Spence (1981).

By taking the complex conjugate of (3.13), and giving close attention to the mode labeling previously noted, it can be shown that

$$\text{if } \beta_q^* = \beta_p, \text{ then } \mathbf{u}_q^* = \mathbf{u}_{-p}.$$

Moreover, by asking that the modes of (3.13) be *symmetric upon reflection in* $x_1 = \text{constant}$, it can be shown that, if $\beta_q^* = \beta_p$, then

$$u_{q\,1}^* = -u_{p\,1}, \; u_{q\,2}^* = u_{p\,2}, \; \tau_{q\,1}^* = \tau_{p\,1}, \; \tau_{q\,2}^* = -\tau_{p\,2}, \; \tau_{q\,3}^* = \tau_{p\,3}. \tag{3.15}$$

The modes are normalized so that the conditions of (3.15) are satisfied. By setting $C_a = C_s = \mathrm{i}$ the eigenmodes $\mathbf{u}_a$ and $\mathbf{u}_s$, (3.3) and (3.4) respectively, are normalized so that these conditions are satisfied.

3.3.2 The sloping boundary

As indicated previously, the presence of a sloping boundary causes some difficulties when formulating the coupled, local mode approximation. Figure 3.2 shows the traction $\mathbf{t}$, where $\mathbf{t} = \hat{n} \cdot \boldsymbol{\tau}$, acting on the surface $x_2 = -h_0 + h_u(\delta x_1)$. The components of the traction are

$$t_1 = \tau_1 \, n_1 + \tau_2 \, n_2, \quad t_2 = \tau_2 \, n_1 + \tau_3 \, n_2,$$

where $\hat{n} = n_1 \hat{e}_1 + n_2 \hat{e}_2$. The eigenmodes used in the coupled-mode approximation are such that $\tau_{2,\,3} = 0$ at both surfaces. However, the exact

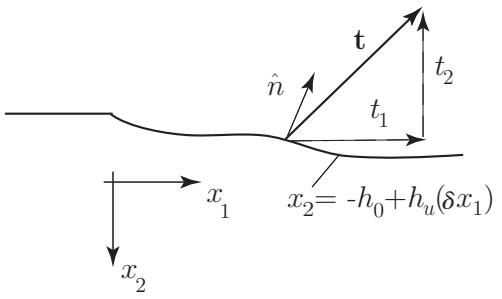

Figure 3.3: The figure shows the traction $\mathbf{t}$ acting on the surface $x_2 = -h_0 + h_u(\delta x_1)$. The component t_1 is discontinuous when local eigenmodes are used to represent it.

boundary conditions ask that $\mathbf{t} = 0$ at the upper, perturbed surface. The coupled-mode eigenmodes do not satisfy this condition because τ_1 is finite at $x_2 = -h_0 + h_u(\delta x_1)$. Thus, when the local eigenmodes are used, a jump in t_1 across the sloping surface is introduced. The finite jump in traction is equivalent to a body force (Hudson 1980, pp. 106–109).

The perturbing function h_u is assumed to be such that

$$dh_u/dx_1 = \delta f(\delta x_1), \quad |f(\delta x_1)| = \mathrm{O}(1),$$

where $\delta \ll 1$, so that $n_1 = \delta f + \mathrm{O}(\delta^3)$ and $n_2 = -1 + \mathrm{O}(\delta^2)$.

The discontinuity in t_1 is equivalent to a body force $-\mathbf{F}$. Therefore, to remove this effect and thereby enforce the true boundary condition, a body force

$$\mathbf{F}(\delta x_1) = -\tau_1 \, \delta f(\delta x_1) \, \delta[x_2 + h_0 - h_u(\delta x_1)] \, \hat{e}_1 + \mathrm{O}(\delta^3), \tag{3.16}$$

is introduced into the problem. The Dirac delta function $\delta(x)$ locates the sloping boundary, and should not be confused with the parameter δ.

3.3.3 Coupled, local modes

The horizontal or lateral variations in the thickness, and therefore the eigenvalues β_p and eigenmodes $\mathbf{u}_p$ depend on the combination δx_1; accordingly, the slow variable $y_1 = \delta x_1$ is introduced everywhere as the independent horizontal variable. A solution to (3.9) is sought subject to the boundary conditions that the traction acting on the surfaces $x_2 = -h_0 + h_u(y_1)$ and $x_2 = h_0$ vanish. The boundary condition at $x_2 = -h_0 + h_u(y_1)$ will be relaxed when determining the local eigenmodes, but enforced on the problem as a whole by introducing the equivalent body force $\mathbf{F}$, given by (3.16).

A solution is sought in the form

$$\mathbf{U} = \sum_{-\infty<r<\infty} \left[c_r(y_1) e^{\mathrm{i}\phi_r(y_1)} \mathbf{u}_r(y_1, x_2) \right], \tag{3.17}$$

where

$$\phi_r(y_1) = \frac{1}{\delta} \int_0^{y_1} \beta_r(y_1') dy_1', \tag{3.18}$$

and $c_0 \equiv 0$. The β_r and $\mathbf{u}_r(y_1, x_2)$ are the eigenvalue and eigenmode of (3.13) at fixed y_1. Recall that a y_1-dependence enters the eigenmodes and eigenvalues through $\bar{x}_2$ and $\bar{h}_0$,.

The sum (3.17) is substituted into (3.9), after which the inner product, (3.14), is taken with $\mathbf{u}_q$, where $\mathbf{u}_q$ is orthogonal to $\mathbf{u}_r \, \forall \, r \neq p$. From (3.14), if $\beta_q^* = \beta_p$, $P_{qp} \neq 0$. This gives the coupled-mode equations

$$\frac{dc_p}{dy_1}(y_1) = -[P_{qp}(y_1)]^{-1} \sum_r \left[c_r(y_1) e^{\mathrm{i}[\phi_r(y_1) - \phi_p(y_1)]} K_{qr}(y_1) \right] + \mathrm{O}(\delta^3). \tag{3.19}$$

Recall, from the discussion of symmetries, that $\mathbf{u}_p = \mathbf{u}_{-q}^*$ when $\beta_q^* = \beta_p$, so that a term with a q subscript can be replaced by one with a p subscript. The interactions among the eigenmodes are represented by the coupling coefficients K_{qr}; these are given as

$$K_{qr}(y_1) = \langle \mathbf{u}_q, \partial_1 \mathbf{u}_r \rangle + \mathrm{i} f(y_1) (u_{q1}^* \, \tau_{r1})_{-h_0 + h_u(y_1)}, \tag{3.20}$$

where $\partial_1 = \partial / \partial y_1$. The last term in (3.20) comes from the body force term given by (3.16). Using the symmetries given by (3.15), it can be shown that

$$K_{qr} = -K_{rq}^*, \;\; \beta_q^* \neq \beta_r. \tag{3.21}$$

Without the body force contribution this symmetry would not be present. It can also be shown that

$$2K_{qr} = \partial_1 P_{qr}, \;\; \beta_q^* = \beta_r. \tag{3.22}$$

To calculate the coupling coefficients it is first noted that

$$\langle \mathbf{u}_q, \partial_1 \left(\mathcal{L} \mathbf{u}_r \right) \rangle = \langle \mathbf{u}_q, \mathcal{L} \left(\partial_1 \mathbf{u}_r \right) \rangle = \mathrm{i} \beta_r \langle \mathbf{u}_q, \partial_1 \mathbf{u}_r \rangle$$

because the parameters in the operator $\mathcal{L}$ are constant and $P_{qr} = 0$. Using (3.12) gives

$$-\mathrm{i}(\beta_q^* - \beta_r) \langle \mathbf{u}_q, \partial_1 \mathbf{u}_r \rangle = -\mathrm{i} (u_{q\,1}^* \, \partial_1 \tau_{r\,2} + u_{q\,2}^* \, \partial_1 \tau_{r\,3})_{-h_0 + h_u(y_1)}.$$

To simplify this expression further the ∂_1 derivatives need to be eliminated. The stress components τ_2, τ_3 are continuous, and 0, along the curve $x_2 = -h_0 + h_u(y_1)$; therefore their derivatives tangent to the boundary curve are also continuous. For these terms

$$\partial_1 = -f(y_1)\,\partial_2,$$

where $\partial_1 = \partial/\partial y_1$, but $\partial_1 = \partial/\partial x_2$. Using these facts and after a lengthy reduction process, the coupling coefficients K_{qr}, for $\beta_q^* \neq \beta_r$, are calculated to be

$$K_{qr}(y_1) = \frac{f(y_1)}{\beta_q^*(y_1) - \beta_r(y_1)} \times \Big[(u_{q1}^* u_{r1} + u_{q2}^* u_{r2}) - c\, u_{q1}^* u_{r1} \beta_q^* \beta_r\Big]_{-h_0+h_u(y_1)}. \tag{3.23}$$

The coupled-mode equations can be put into another more compact form. From this point forward it will be assumed that *the only eigenvalues of interest are real*. These are the eigenvalues that correspond to propagating waves and are thus the ones of most interest. Define

$$q_p := c_p P_{pp}^{1/2},$$

and

$$Q_{pr} := \frac{K_{pr}\,(\beta_p - \beta_r)}{f\, P_{pp}^{1/2} P_{rr}^{1/2}}.$$

All that is being done is to renormalize each local mode $\mathbf{u}_p$ with $P_{pp}^{1/2}$. Note that P_{pp} depends on y_1, see (3.14) and (3.11). The coupled mode equations (3.19) now take the form

$$\frac{dq_p}{dy_1} = f(y_1) \sum_{\{r\,|\,\beta_r \text{ real}\}} (\delta_{rp} - 1) q_r(y_1) e^{i[\phi_r(y_1) - \phi_p(y_1)]}\, \frac{Q_{pr}(y_1)}{\beta_p(y_1) - \beta_r(y_1)}. \tag{3.24}$$

Recall that $q_0 \equiv 0$. The term δ_{rp} is the Kronecker delta. Overall this result is very satisfying because its form makes transparent the nature of the off-diagonal coupling: The perturbation f causes the coupling, the difference $\beta_p - \beta_r$ suggests which modes are engaged most strongly, and the Q_{pr} measure the strength of the coupling.

3.4 Coupling of the two lowest Rayleigh-Lamb modes

Recall the problem with which the chapter began: The two lowest Rayleigh-Lamb modes are excited in the uniform region of the layer in Figure 3.1, and are incident on the nonuniform region, to the right. What is the effect of the variable change in thickness on the propagation?

Harris and Block (2005) have examined (3.24) in detail. The outcome is that for the initial conditions

$$q_{1,\,2}(0) \neq 0, \quad q_p(0) = 0 \;\forall\, p \neq 1, 2\,, \tag{3.25}$$

provided $|\beta_p - \beta_q| \neq \mathrm{O}(\delta)$ the propagation is adiabatic in the sense that

$$q_{1,\,2}(y_1) = q_{1,\,2}(0) + \mathrm{O}(\delta), \quad q_p(y_1) = \mathrm{O}(\delta) \;\forall\, p \neq 1, 2\,, \tag{3.26}$$

because the coupling coefficient

$$\frac{f(y_1) Q_{pr}(y_1)}{\beta_p(y_1) - \beta_r(y_1)}.$$

varies slowly. This is the assumption made by Folguera and Harris (1999). However, it breaks down when ϵ is of the same order as δ. From (3.7) and Figure 3.2 this happens when $\bar{h}_0$ is large.

3.4.1 A matrix WKBJ approximation

Therefore the coupled-mode equations (3.24) can be truncated to only two equations, namely those for the two eigenmodes $\mathbf{u}_a$, (3.3), and $\mathbf{u}_s$, (3.4). Note that the subscript 1 is now being replaced by a for the lowest antisymmetric mode and 2 by s for lowest symmetric one. Therefore the sum (3.17) is approximated as

$$\mathbf{U} \approx \sum_{r=a,s} \left[q_r(y_1) e^{\mathrm{i}\phi_r(y_1)} \frac{\mathbf{u}_r(y_1, x_2)}{P_{rr}^{1/2}(y_1)} \right], \tag{3.27}$$

where $\phi_{a,s}$ is given by (3.18) using $\beta_{a,s}$. This equation is also a modification of (3.8) to the case of a laterally inhomogeneous guide, with $q_{a,\,s}$ to be determined. It remains to truncate (3.24) to calculate them.

Writing

$$\mathbf{q}(y_1) := [q_a(y_1), q_s(y_1)]^T,$$

the coupled-mode equations become

$$-\mathrm{i}\,\delta \frac{d\mathbf{q}}{dy_1} = \mathbf{B}(y_1) \cdot \mathbf{q}\,, \tag{3.28}$$

where

$$\mathbf{B}(y_1) = \mathrm{i}\, f(y_1) \begin{bmatrix} 0 & \dfrac{\delta\, Q(y_1)}{2\epsilon(y_1)}\, e^{-\mathrm{i}\frac{2}{\delta}\int_a^{y_1} \epsilon(y_1')\, dy_1'} \\ -\dfrac{\delta\, Q(y_1)}{2\epsilon(y_1)} e^{\mathrm{i}\frac{2}{\delta}\int_a^{y_1} \epsilon(y_1')\, dy_1'} & 0 \end{bmatrix}. \tag{3.29}$$

For the moment it is assumed that $\delta/\epsilon = \mathrm{O}(1)$. The case where $\delta/\epsilon \ll 1$ can be recovered from the asymptotic approximation to (3.29). However, the limit $\epsilon \to 0$ cannot easily be recovered from this approximation; therefore, it is assumed that $\epsilon \neq 0$. Note that this matrix equation has the general form that invites a WKBJ approximation applied to the two modes together, rather than to each singly. As well, using the symmetries indicated by (3.15), note that $Q_{as} = Q_{sa} = Q$. The matrix $\mathbf{B}$ is Hermitian and thus has two linearly independent eignvectors.

The initial condition is given by (3.25). Following Fedoryuk (1993, pp. 42–45, 64–65), a WKBJ solution to (3.28) of the form

$$\mathbf{q} = e^{\mathrm{i}\Theta/\delta} \sum_{n\geq 0} \delta^n \left[A_{1n}, A_{2n} e^{-\mathrm{i}\frac{2}{\delta}\int_0^{y_1} \epsilon\, dy_1'} \right]^T$$

is sought. Setting

$$\frac{d\Theta}{dy_1} = \lambda,$$

the first term leads to the eigenvalue problem:

$$\begin{bmatrix} 0 & \mathrm{i}\dfrac{\delta}{2\epsilon}\, f\, Q \\ -\mathrm{i}\dfrac{\delta}{2\epsilon}\, f\, Q & -2\epsilon \end{bmatrix} \begin{bmatrix} A_{01} \\ \\ A_{02} \end{bmatrix} = \lambda \begin{bmatrix} A_{01} \\ \\ A_{02} \end{bmatrix}.$$

The eigenvalues $\lambda^{\pm}$ are

$$\lambda^{\pm} = -\epsilon \pm \left(\epsilon^2 + \frac{\delta^2}{4\epsilon^2}\, f^2\, Q^2 \right)^{1/2}, \tag{3.30}$$

and the two orthogonal eigenvectors are

$$[A_{01},\, A_{02}]^{\pm} = C^{\pm}(y_1) \left[\mathrm{i}\frac{\delta}{2\epsilon}\, fQ,\, \lambda^{\pm} \right].$$

Lastly

$$\Theta^{\pm} = -\int_0^{y_1} \epsilon \, dy_1' \pm \int_0^{y_1} \left(\epsilon^2 + \frac{\delta^2}{4\epsilon^2} \, f^2 \, Q^2 \right)^{1/2} dy_1'.$$

The $C^{\pm}$ are found by looking at the equations governing the next order; namely

$$\begin{bmatrix} -\lambda & \mathrm{i}\dfrac{\delta}{2\epsilon} \, f \, Q \\ -\mathrm{i}\dfrac{\delta}{2\epsilon} \, f \, Q & -(\lambda + 2\epsilon) \end{bmatrix} \begin{bmatrix} A_{11} \\ A_{12} \end{bmatrix} = \begin{bmatrix} -\mathrm{i} \, \dfrac{dA_{01}}{dy_1} \\ -\mathrm{i} \, \dfrac{A_{02}}{dy_1} \end{bmatrix}.$$

For $\lambda^{\pm}$, the right-hand side must be orthogonal to $\mathbf{A}_0^{\pm}$. This gives first order differential equations for the $C^{\pm}$ that are readily solved.

The outcome is:

$$\begin{aligned} \mathbf{q}(y_1) = & \frac{C^+(0)}{\left[(\lambda^+)^2 + \frac{\delta^2}{4\epsilon^2} \, f^2 \, Q^2 \right]^{1/2}} \, \mathbf{E}^+ \, e^{\frac{\mathrm{i}}{\delta} \int_0^{y_1} \left(\epsilon^2 + \frac{\delta^2}{4\epsilon^2} \, f^2 \, Q^2 \right)^{1/2} dy_1'} \\ & + \frac{C^-(0)}{\left[(\lambda^-)^2 + \frac{\delta^2}{4\epsilon^2} \, f^2 \, Q^2 \right]^{1/2}} \, \mathbf{E}^- \, e^{-\frac{\mathrm{i}}{\delta} \int_0^{y_1} \left(\epsilon^2 + \frac{\delta^2}{4\epsilon^2} \, f^2 \, Q^2 \right)^{1/2} dy_1'} \\ & + \mathrm{O}(\delta) \, . \end{aligned} \tag{3.31}$$

The vectors $\mathbf{E}^{\pm}$ are given by

$$\mathbf{E}^{\pm} = \begin{bmatrix} \mathrm{i}\frac{\delta}{2\epsilon} \, f \, Q \, e^{-(\mathrm{i}/\delta) \int_0^{y_1} \epsilon \, dy_1'} \\ \lambda^{\pm} \, e^{(\mathrm{i}/\delta) \int_0^{y_1} \epsilon \, dy_1'} \end{bmatrix}. \tag{3.32}$$

The $\lambda^{\pm}$ are given by (3.30), and the Q are calculated from (3.23). The terms $\lambda^{\pm}$, Q, f, and ϵ are all functions of y_1.

To impose the initial conditions (3.25) a decision as to the nature of $f(0)$ must be made. To ensure that the stress terms in the mode vector remain continuous, the perturbed surface must blend smoothly into the uniform one; $f(0) = 0$ enforces this (a weaker condition is sometimes possible). Taking a limit as $y_1 \to 0$ gives

$$C^+(0) = -\mathrm{i} q_1(0), \quad C^-(0) = q_2(0). \tag{3.33}$$

Fedoryuk (1993, pp. 42–45, 64–65) indicates how to calculate additional terms to (3.31). It is shown there that the second-order terms contain the factor $(\lambda^+ - \lambda^-)^{-1}$.

3.4.2 Discussion of the WKBJ approximation

Equations (3.31)–(3.33) give a solution for all $delta/\epsilon$ up to the limit that this ratio is of order one. As δ/ϵ grows small,

$$\lambda^+ \approx \frac{\delta^2}{8\epsilon^3} f^2\, Q^2, \quad \lambda^- \approx -2\epsilon.$$

causing the the combination $f\,Q$ to disappear from (3.31) and (3.32) and the adiabatic approximation (3.26) to be recovered. This is the case considered by Folguera and Harris (1999). The present calculation extends that work to cases where $\delta/\epsilon = \mathrm{O}(1)$. In this case both ϵ and $f\,Q$ contribute to the phase differences between the two modes. If propagation from a thick to a thinner section is considered, then a wave that approximates a Rayleigh surface-wave on the upper surface progressively separates into the two lowest Rayleigh-Lamb modes; the wave numbers of these two modes become separated by $2\epsilon = \epsilon_a + \epsilon_s$ as indicated by Figure 3.2. In this case ϵ is no longer approximated by (3.7). If propagation from a thin to a thicker section is considered, then the wavenumbers of two lowest Rayleigh-Lamb modes coalesce; the sum of the two modes forms a modulated Rayleigh surface-wave. The initial conditions (3.25) have been taken to be such that this Rayleigh wave propagates on the upper perturbed surface.

However, this calculation does not allow one to take the limit $\bar{h}_0 \to \infty$, or equivalently, $\epsilon \to 0$. In this case the coupling coefficient K_{qr}, given first by (3.20), cannot be calculated. One must return to the original expansion (3.17) and construct it of combinations of $\mathbf{u}_a$ and $\mathbf{u}_s$ such that coupling coefficients, that do not become indefinite, can be defined. This calculation remains to be made.

3.5 Summary

This chapter has in some sense been left incomplete. Much numerical work needs to be done to understand completely the consequences of the many equations given here. Nevertheless, it is remarkable that so much progress can be made using asymptotic methods. Moreover, there are several global ideas from this work that can be carried forward to other guided-wave problems.

1. Equations (3.9)–(3.14) provide a framework within which to address waveguiding problems. In particular, using the operator $\mathcal{L}$, rather than working with second-order equations for the particle displacements or for potentials, greatly facilitates the work.

2. The coupled-mode approximation reduces the solution of propagation in laterally inhomogeneous environments to solving an infinite system of coupled ordinary differential equations of the general form

$$d\mathbf{q}/dx = \mathbf{A}(x, \delta) \cdot \mathbf{q},$$

where δ is a small parameter. A knowledge of the behavior of the coupling coefficients sometimes allows the system to be truncated to a very small system. Many interesting applications to wave propagation using systems of equations of this general form remain to be explored.

Appendix A

A miscellany

A.1 Linear elasticity

One often cited textbook describing linear elastodynamics is Achenbach (1973), while a second useful one is Hudson (1980). In both cases the introduction to elasticity is concise but complete. The first volume of the textbooks by Auld (1990b) is insightful, though its approach is somewhat unconventional, and the notation has not been widely adopted in mechanics.

For the present purposes it is enough to work with Cartesian coordinates, using a subscript notation such that $i = 1, 2, 3$ or $i, j = 1, 2, 3$. It is assumed that summation takes place over repeated indices. The coordinates are x_i; a vector, when not represented as $\mathbf{u}$, is represented as u_i; and a tensor, when not represented as $\boldsymbol{\tau}$, is represented as τ_{ij}. There is an underlying orthonormal set of basis vectors $\hat{e}_i$, $i = 1, 2, 3$.

When working in two dimensions the roman subscripts are often replaced by greek ones. The coordinates are x_α, a vector is u_α and a tensor is $\tau_{\alpha\beta}$. In these cases $\alpha, \beta = 1, 2$.

The conservation of linear and angular momentum is expressed as

$$\partial_k \tau_{ki} + \rho_s f_i = \rho_s \partial_t^2 u_i, \quad \tau_{ij} = \tau_{ji}\,. \tag{A.1}$$

The constitutive relation is

$$\tau_{ij} = \lambda_s \partial_k u_k \delta_{ij} + 2\mu \epsilon_{ij}, \quad \epsilon_{ij} = (\partial_i u_j + \partial_j u_i)/2\,. \tag{A.2}$$

Using the two previous equations, the equation of motion becomes

$$(\lambda_s + \mu)\partial_i \partial_k u_k + \mu \partial_j^2 u_i + \rho_s f_i = \rho_s \partial_t^2 u_i. \tag{A.3}$$

This equation can be rearranged using the vector identity

$$\nabla^2\mathbf{A} = \nabla(\nabla\cdot\mathbf{A}) - \nabla\wedge(\nabla\wedge\mathbf{A}).$$

By setting

$$\mathbf{u} = \nabla\varphi + \nabla\wedge\boldsymbol{\psi}, \quad \nabla\cdot\boldsymbol{\psi} = 0,$$

and

$$\mathbf{f} = c_L^2\nabla F + c_T^2\nabla\wedge\mathbf{G},$$

the equation of motion (A.3) can be reduced to the pair

$$\nabla^2\varphi + F = c_L^{-2}\partial_t^2\varphi, \quad \nabla^2\boldsymbol{\psi} + \mathbf{G} = c_T^{-2}\partial_t^2\boldsymbol{\psi}. \tag{A.4}$$

In (A.1)–(A.4) the particle displacement is $\mathbf{u}$, the stress tensor $\boldsymbol{\tau}$, the strain tensor $\boldsymbol{\epsilon}$, and the body force per unit mass $\mathbf{f}$. The material parameters are the density ρ_s, and the Lamè parameters λ_s and μ. Throughout this monograph these parameters are constant. The longitudinal and shear wavespeeds are

$$c_L = [(\lambda_s + 2\mu)/\rho_s]^{1/2}, \quad c_T = (\mu/\rho_s)^{1/2},$$

respectively. The subscript s indicates that the parameter describes a property of a solid. The symbols $\partial_i := \partial/\partial x_i$, $\partial_t := \partial/\partial t$, and $\partial_i^2 := \partial^2/\partial x_i^2$. In two dimensions ∂_α would be used. Equation (A.4) indicates that two types of wave propagate in a linearly elastic solid, namely, a compressional (φ) wave and a shear ($\boldsymbol{\psi}$) wave. In the plane-wave limit these become a longitudinal wave and a transverse wave, respectively.

A.2 Linear acoustics

Both Morse and Ingard (1968) and Pierce (1981) describe the equations of linear acoustics, though Pierce connects them more thoroughly with the underlying Navier-Stokes equations. Because only ideal fluids are considered, that is fluids having no viscosity, and only the linear equations are needed, the acoustic equations are given here in a form that indicates their parallelism with those of linear elasticity.

It is useful to note that the conservation of mass, in the linear approximation, is

$$\rho_f' = \rho_f(1 - \epsilon_{kk}), \quad \epsilon_{kk} = \nabla\cdot\mathbf{u},$$

the prime indicating the density after the fluid is perturbed from its ambient state. This relation is not used elsewhere in this work, but is used in most textbooks discussing linear acoustics.

The conservation of linear and angular momentum is again expressed by (A.1), with ρ_s replaced by ρ_f. In addition there is the kinematic constraint

$$\nabla \wedge \mathbf{u} = 0.$$

The stress is given as

$$\tau_{ij} = -p\delta_{ij},$$

where the acoustic pressure

$$p = -\lambda_f \nabla \cdot \mathbf{u}.$$

The constitutive relation is thus expressed by (A.2) with μ set to zero and λ_s replaced by λ_f. As should be apparent, the subscript f indicates that the parameter describes a fluid property. The equation of motion becomes

$$\lambda_f \partial_k \partial_k u_i + \rho_f f_i = \rho_f \partial_t^2 u_i. \tag{A.5}$$

By setting $\mathbf{u} = \nabla\varphi$ and $\mathbf{f} = c^2 \nabla F$, the equation of motion can be written as

$$\nabla^2 \varphi + F = c^{-2} \partial_t^2 \varphi, \tag{A.6}$$

where $c = (\lambda_f/\rho_f)^{1/2}$. Note that

$$p = -\rho_f \partial_t^2 \varphi.$$

A.3 Continuity and boundary conditions

Consider a plane fluid-solid interface oriented by means of a unit normal vector $\hat{n}$ pointing into the fluid. Figure 1.1 indicates the geometry. The fluid is ideal so that the no-slip condition is *not* enforced. The traction acting on the surface of the solid is $\mathbf{t_s} = \hat{n} \cdot \boldsymbol{\tau}$. The continuity conditions at the interface are thus expressed as

$$\mathbf{t}_s \cdot \hat{n} = -p_f, \quad \hat{n} \wedge \mathbf{t}_s = 0, \quad \mathbf{u}_s \cdot \hat{n} = \mathbf{u}_f \cdot \hat{n}. \tag{A.7}$$

The only other boundary condition needed in this work is one at infinity. The waves must in general be outgoing, though when the focused beam is discussed an incoming wave is considered. The *principle of limiting absorption* (Harris 2001, pp. 62,63) is used to determine this. Either by Fourier transforming a signal or by considered a time-harmonic one, in the far-field, it will have the form

$$\varphi = \frac{A(\phi, \theta)}{kr} e^{\mathrm{i}(kr - \omega t)},$$

where (r, ϕ, θ) are spherical coordinates, and $k = \omega/c$ is the wavenumber, with c being the wavespeed. The angular frequency is defined such that $\omega = \omega_0 + \mathrm{i}\epsilon$, $\omega_0 > 0$, $\epsilon \geq 0$. The wavenumber then becomes $k = (\omega_0/c) + \mathrm{i}(\epsilon/c)$. Therefore

$$|\varphi| \sim e^{-\epsilon r/c}\, e^{\epsilon t},\ r \to \infty,$$

and t is fixed; that is, the wave vanishes provided the combination $\mathrm{i}(kr - \omega t)$ appears in some guise. The parameter ϵ can be sent to zero at the end of the calculations.

A.4 Piezoelectric coupling and an electromechanical reciprocity relation

Transducers operating at microwave frequencies frequently use piezoelectric coupling to convert electrical to mechanical signals and vice versa. While the equations of piezoelectricity are not explicitly used in this work, an electromechanical reciprocity identity, that assumes the coupling is piezoelectric, is used, and its use is central to the writer's arguments. Hence to sketch its derivation a summary of the equations of linear piezoelectricity is needed. A description of piezoelectricity can be found in Auld (1990b, pp. 265–298). The electromechanical reciprocity identity itself is also derived in Auld (1990a, pp. 153,154), and is further discussed in Achenbach (2003, pp. 233–246).

Maxwell's equations

$$e_{ijk}\partial_j E_k + \partial_t B_i = 0, \quad e_{ijk}\partial_j H_k - \partial_t D_i = J_i,$$

are coupled with (A.1) through the constitutive relations

$$D_i = \kappa_{ij} E_j + \rho_{ijk}\epsilon_{jk},$$
$$\tau_{ij} = -\rho_{ijk} E_k + c_{ijkl}\epsilon_{kl}.$$

The permutation symbol e_{ijk} is defined as

$$e_{ijk} = \begin{cases} +1 & \text{if } (i,j,k) \text{ are all unequal and in cyclic order} \\ -1 & \text{if } (i,j,k) \text{ are all unequal and not in cyclic order} \\ 0 & \text{if any two of } (i,j,k) \text{ are equal.} \end{cases}$$

In addition $B_i = \nu H_i$. The terms $\mathbf{E}, \mathbf{B}, \mathbf{H}$ and $\mathbf{D}$ are the electric intensity, the magnetic induction, the magnetic intensity, and electric displacement. The vector $\mathbf{J}$ is an imposed current; the materials themselves are assumed

to be nonconducting. Piezoelectric materials must be anisotropic; thus, the various coupling parameters are tensors of the order indicated by their subscripts. κ_{ij} are the dielectric coefficients, ρ_{ijk} the piezoelectric coefficients, and c_{ijkl} the elastic coefficients. ν is the magnetic permeability. All the coefficients are assumed to be constant.

Using thermodynamics and the symmetry of $\boldsymbol{\tau}$, it can be shown that

$$\begin{gathered} c_{ijkl} = c_{klij},\ c_{ijkl} = c_{jikl}, \\ \rho_{ikl} = \rho_{kli},\ \rho_{ijk} = \rho_{jik}, \\ \kappa_{ij} = \kappa_{ji}. \end{gathered}$$

Other symmetries can be derived from these.

Let $(\mathbf{E}^1, \mathbf{H}^1, \boldsymbol{\tau}^1, \mathbf{u}^1)$ and $(\mathbf{E}^2, \mathbf{H}^2, \boldsymbol{\tau}^2, \mathbf{u}^2)$ be two electromechanical states that satisfy the previously listed equations. Moreover, assume that $\partial_t \to -\mathrm{i}\omega$. In essence, the equations satisfied by state 1 are multiplied by the variables of state 2, and the equations satisfied by state 2 are multiplied by the variables of state 1; the equations are then added or subtracted to remove common terms; and then combined in a way that gives a divergence on one side and forcing terms on the other. The only point to note is that it is the particle velocity $-\mathrm{i}\omega\mathbf{u}$, rather than the particle displacement, that is needed. The result of these operations is the following reciprocity identity:

$$\begin{aligned} \partial_i \left[-\mathrm{i}\omega(u_j^1 \tau_{ij}^2 - u_j^2 \tau_{ij}^1) + e_{ijk}(E_j^1 H_k^2 - E_j^2 H_k^1) \right] \\ = -\mathrm{i}\omega\rho_s(u_j^2 f_j^1 - u_j^1 f_j^2) + (E_j^2 J_j^1 - E_j^1 J_j^2). \end{aligned} \quad \text{(A.8)}$$

A.5 Notes on Hankel functions

The following facts are taken from Magnus, Oberhettinger, and Soni (1966); the section numbers refer to this handbook.

1. From §3.1.2: The principal branch for the Hankel functions $H_0^{(1)}(z)$ and $H_0^{(2)}(z)$ is defined by $\arg(z) \in (-\pi, \pi)$. The connections among the branches are

   $$H_0^{(1)}(ze^{\mathrm{i}\pi}) = -H_0^{(2)}(z), \quad H_0^{(2)}(ze^{-\mathrm{i}\pi}) = -H_0^{(1)}(z).$$

   Hankel functions are used in several places; however, their branch cuts are not always explicitly shown in the diagrams of the complex plane.

2. From §3.6.4: Sommerfeld's integral representations for the Hankel functions are:

$$H_0^{(1)}(z) = \frac{1}{\pi}\int_{\mathcal{C}_1} e^{\mathrm{i}z\cos\mu}d\mu,$$

and

$$H_0^{(2)}(z) = \frac{1}{\pi}\int_{\mathcal{C}_2} e^{-\mathrm{i}z\cos\mu}d\mu.$$

The contour $\mathcal{C}_1$ starts at $-\pi/2+\mathrm{i}\infty$ and ends at $\pi/2-\mathrm{i}\infty$; the contour $\mathcal{C}_2$ starts at $-\pi/2-\mathrm{i}\infty$ and ends at $\pi/2+\mathrm{i}\infty$; and $\Re(z) > 0$. These two integral representations can be combined to show that

$$J_0(z) = \frac{1}{2\pi}\int_0^{2\pi} e^{\mathrm{i}z\cos\mu}d\mu,$$

a result that can be arrived at in several other ways.

3. From §3.14.1: Asymptotic expansions for the Hankel functions are

$$H_0^{(1),(2)}(z) \sim (\pi z/2)^{-1/2}e^{\pm\mathrm{i}(z-\pi/4)},\ |z|\to\infty, \tag{A.9}$$

where, for the (1) function $\arg z \in (-\pi, 2\pi)$, and for the (2) function $\arg z \in (-2\pi, \pi)$.

One additional fact is of use. There is a Parseval's relation between functions and their Hankel transforms (Sneddon 1951, pp. 59,60). The Hankel transform pair are given as

$$^*f(u) = \int_0^\infty yf(y)J_0(uy)dy,$$
$$f(x) = \int_0^\infty u\,^*f(y)J_0(xu)du;$$

and the Parseval's relation is

$$\int_0^\infty xf(x)g(x)dx = \int_0^\infty u\,^*f(u)\,^*g(u)du. \tag{A.10}$$

Works Cited

Achenbach, J. D. 1973. *Wave Propagation in Elastic Solids*. Amsterdam: North-Holland.

———. 2003. *Reciprocity in Elastodynamics*. New York: Cambridge.

Auld, B. A. 1979. General electromechanical reciprocity relations applied to the calculation of elastic wave scattering coefficients. *Wave Motion* 1:3–10.

———. 1990a. *Acoustic Fields and Waves in Solids*. Second edition. Volume 2. Malabar, FL: Krieger.

———. 1990b. *Acoustic Fields and Waves in Solids*. Second edition. Volume 1. Malabar, FL: Krieger.

Berry, M. V., and K. E. Mount. 1972. Semiclassical approximations in wave mechanics. *Rep. Prog. Phys* 35:315–397.

Besserer, H., and P. G. Malischewsky. 2004. Mode series expansions at vertical boundaries in elastic waveguides. *Wave Motion* 39:41–59.

Born, M., and E. Wolf. 1999. *Principles of Optics*. Seventh (expanded) edition. Cambridge: Cambridge University Press.

Brekhovskikh, L. M., and O. A. Godin. 1999. *Acoustics of Layered Media*. Second edition. Volume 2. Berlin: Springer-Verlag.

Brekhovskikh, L. M., and V. Goncharov. 1985. *Mechanics of Continua and Wave Dynamics*. Berlin: Springer-Verlag.

Briggs, A. 1992. *Acoustic Microscopy*. New York: Oxford University Press.

Budden, K. G. 1975. The critical coupling of modes in a tapered earth-ionosphere wave guide. *Math. Proc. Camb. Phil. Soc.* 77:567–580.

Budden, K. G., and M. Eve. 1975. Degenerate modes in the earth-ionosphere waveguide. *Proc. R. Soc. Lond.* A 342:175–190.

Ciarkowski, A. 1989. Uniform asymptotic expansion of an integral with a saddle point, a pole and a branch cut. *Proc. R. Soc. Lond.* A 426:273–286.

Clemmow, P. C. 1966. *The Plane Wave Spectrum Representation of Electromagnetic Waves*. Oxford: Pergamon.

Collin, R. E. 1991. *Field Theory of Guided Waves*. Second edition. New York: IEEE Press.

Fedoryuk, M. V. 1993. *Asymptoic Analysis*. Berlin: Springer Verlag.

Felsen, L. B., and N. Marcuvitz. 1994. *Radiation and Scattering of Waves*. New York: IEEE and Oxford University Press.

Folguera, A., and J. G. Harris. 1999. Coupled Rayleigh surface waves in a slowly varying elastic waveguide. *Proc. R. Soc. Lond.* A 455:917–931.

Harris, J. G. 1989. An asymptotic description of an elastodynamic beam. Edited by M. F. McCarthy and M. A. Hayes, *Elastic Wave Propagation*. Amsterdam: North-Holland, 505–510.

———. 1997. Modeling scanning acoustic imaging of defects at solid interfaces. Edited by G. Chavent, G. Papanicolaou, P. Sacks, and W. W. Symes, *Inverse Problems in Wave Propagation*. New York: Springer, 237–257.

———. 2001. *Linear Elastic Waves*. New York: Cambridge University Press. A list of errors is maintained at www.diffractedwave.com.

Harris, J. G., and G. Block. 2005. The coupling of elastic, surface-wave modes by a slow, interfacial inclusion. Preprint available.

Harris, J. G., and J. Pott. 1985. Further studies of the scattering of an acoustic Gaussian beam from a fluid-solid interface. *J. Acoust. Soc. Am.* 78:1072–1080.

Heading, J. 1962. *An Introductionto Phase-Integral Methods*. London: Methuen.

Herrara, I., and D. A. Spence. 1981. Framework of biorthogonal series. *Proc. Nat. Acad. Sci. Am.* 78:7240–7244.

Hudson, J. A. 1980. *The Excitation and Propagation of Elastic Waves*. Cambridge: Cambridge University Press.

Jeffreys, H. 1962. *Asymptotic Approximations*. Oxford: Clarendon Press.

Kennett, B. L.N. 1984. Guided wave propagation in laterally varying media I. Theoretical development. *Geophys. J. R. Astr. Soc.* 79:235–255.

Kirrmann, P. 1995. On the completeness of Lamb modes. *J. Elasticity* 37:39–69.

Liang, K. K., G. S. Kino, and B. T. Khuri-Yakub. 1985. Material characterization by the inversion of $V(z)$. *IEEE Trans. Sonics Ultrason.* SU 32:213–224.

Magnus, W., F. Oberhettinger, and R. P. Soni. 1966. *Formulas and Theorems for the Special Functions of Mathematical Physics.* Third enlarged edition. New York: Springer-Verlag.

Malischewsky, P. 1987. *Surface Waves and Discontinuities.* Berlin: Akademie-Verlag.

Maupin, V. 1988. Surface waves across 2-D structures: a method based on coupled local modes. *Geophys. J.* 93:173–185.

Miklowitz, J. 1978. *Elastic Waves and Waveguides.* Amsterdam: North-Holland.

Morse, P. M., and K. U. Ingard. 1968. *Theoretical Acoustics.* New York: McGraw-Hill.

Pierce, A. D. 1981. *Acoustics.* New York: McGraw-Hill.

Pott, J., and J. G. Harris. 1984. Scattering of an acoustic Gaussian beam from a fluid-solid interface. *J. Acoust. Soc. Am.* 76:1829–1838.

Rebinsky, D. A. 1991. Asymptotic description of the acoustic microscopy of a surface-breaking crack. Ph.D. diss., University of Illinois, Urbana-Champaign.

Rebinsky, D. A., and J. G. Harris. 1992a. The acoustic signature for a surface-breaking crack produced by a point focus microscope. *Proc. R. Soc. Lond.* A 438:47–65.

———. 1992b. An asymptotic calculation of the acoustic signature of a cracked surface for the line focus scanning acoustic microscope. *Proc. R. Soc. Lond.* A 436:251–265.

Rutherford, S. R., and K. E. Hawker. 1981. Consistent coupled mode theory of sound propagation for a class of nonseperable problems. *J. Acoust. Soc. Am.* 70:554–564.

Shevchenko, V. V. 1971. *Continuous Transitions in Open Waveguides.* Boulder, CO: Golem press.

Sneddon, I. N. 1951. *Fourier Transforms.* New York: McGraw-Hill.

Somekh, M. G., H. L. Bertoni, G. A. D. Briggs, and N. J. Burton. 1985. A two-dimensional imaging theory of surface discontinuities with the scanning acoustic microscope. *Proc. R. Soc. Lond.* A 401:29–51.

Steele, C. R. 1976. Application of the WKB method in solid mechanics. Edited by S. Nemat-Nasser, *Mechanics Today*, Volume 3. New York: Pergamon, 243–295.

Ti, B. W., W. D. O'Brien, and J. G. Harris. 1997. Measurement of coupled wave propagation in an elastic plate. *J. Acoust. Soc. Am.* 102:1528–1531.

Wasow, W. 1987. *Asymptotic Expansions for Ordinary Differential Equations*. New York: Dover.

Index

F-number, 15

acoustic material signature, 29, 31
acoustics, equations of linear, 2, 52
angular spectrum of plane waves, 4

continuity conditions, fluid-solid interface, 3, 53
coupled modes, 37, 44, 46
coupling, Rayleigh-Lamb modes, 46
critical coupling, 36, 49

degenerate modes, 36
dispersion curves, lowest Rayleigh-Lamb modes, 36
dispersion relation, Rayleigh-Lamb, 38

eigenvalue problem, 41
elasticity, equations of linear, 2, 51
electromechanical reciprocity identity, 26, 55
equivalent body force, 43

focused beam, converging reflected, 25
focused beam, diverging reflected, 22
focused beam, representations, 18
focused beam, scattered, 20
Fresnel number, 15

Hankel functions, assorted results, 55

imaging equation, 30
invariant embedding, 37

jump in traction, 43

limiting absorption, principle of, 53

measurement model, 26, 28
microscope, acoustic reflection, imaging equation, 30
microscope, acoustic reflection, qualitative description, 13
modes, local coupled, 37, 44, 46

piezoelectricity, equations of, 54
polarization vector, 5
propagation vector, 5

Rayleigh wave, focusing, 25
Rayleigh wave, leaky, 10
Rayleigh wave, leaky, filling lens' aperture, 22
Rayleigh-Lamb modes, 34, 38
Rayleigh-Lamb modes, dispersion curves, 36
reflected plane wave, 5
reflected spherical wave, asymptotic approximation, 7, 9
reflection coefficient, 6
reflection coefficient, poles and branch points of, 7
reflection, measured at transducer, 28

Riemann sheet, the physical, 9, 20, 21

scattered waves, from a fluid-solid interface, 6
spherical wave, converging, 17
spherical wave, representation in terms of cylindrical waves, 4
spherical wave, representation in terms of plane waves, 4
spherical wave, specularly reflected, 9
symmetries, waveguide eigenmodes, 42

transmission coefficient, 6
transmitted plane waves, 5

WKBJ approximation, 37, 47